

# TABLE OF CONTENTS

	<u>Page</u>	
CHAPTER 1	1	1/A10
CHAPTER 2	5	1/A14
2.1	5	1/A14
2.2	13	1/B8
2.3	21	1/C2
CHAPTER 3	24	1/C5
3.1	24	1/C5
3.2	28	1/C9
CHAPTER 4	43	1/D10
CHAPTER 5	45	1/D12
CHAPTER 6	53	1/E6
CHAPTER 7	56	1/E9
CHAPTER 8	59	1/E12
8.1	59	1/E12
8.2	61	1/E14
CHAPTER 9	70	1/F3
9.1	70	1/F9
9.2	71	1/F10
CHAPTER 10	80	1/G5
10.1	80	1/G5
10.2	81	1/G6
10.3	82	1/G7
10.4	82	1/G7
10.5	86	1/G11
10.6	88	1/G13
CHAPTER 11	94	2/A11
REFERENCES	96	2/A13

# LIST OF FIGURES

<u>Figure</u>		<u>Page</u>
1.	NO versus Time for Stoichiometric Burned Gas at Various Temperatures; pressure = 15 atm; fuel=kerosene; dashed lines are equilibrium levels from Heywood, et. al. (11) . . . . .	12 1/B7
2.	Characteristic Time for NO Formation versus Equivalence Ratio for Various Engine Pressure Ratios; see Table 3 for inlet conditions. . . . .	12 1/B7
3.	Rate of Increase in NO <sub>x</sub> Emission Index versus Mean Equivalence Ratio for Various Values of Nonuniformity Parameter, 8:1 Engine Pressure Ratio; see Table 3 for inlet conditions. . . . .	14 1/B9
4.	Rate of Increase in NO <sub>x</sub> Emission Index versus Mean Equivalence Ratio for Various Values of Nonuniformity Parameter, 16:1 Engine Pressure Ratio; see Table 3 for inlet conditions. . . . .	18 1/B13
5.	Rate of Increase in NO <sub>x</sub> Emission Index versus Mean Equivalence Ratio for Various Values of Nonuniformity Parameter, 24:1 Engine Pressure Ratio; see Table 3 for inlet conditions. . . . .	18 1/B13
6.	Rate of Increase in NO <sub>x</sub> Emission Index versus Mean Equivalence Ratio for Various Values of Nonuniformity Parameter, 32:1 Engine Pressure Ratio; note NO <sub>x</sub> scale shift from previous figures; see Table 3 for inlet conditions . . . . .	19 1/B14
7.	Comparison of NO <sub>x</sub> Predictions with Premixed Experimental Data, 800 K Inlet; pressure = 5.5 atm; s = 0 for curve A, s = 0.1 for curve B; data from Anderson (15). . . . .	26 1/C7
8.	Comparison of NO <sub>x</sub> Predictions with Premixed Experimental Data, 600 K Inlet; see text for details . . . . .	26 1/C7
9.	Details of NASA Swirl-Can Module. . . . .	30 1/C11
10.	Tangential View of NASA Swirl-Can Combustor Annulus . . . . .	30 1/C11
11.	Comparison of NO <sub>x</sub> Predictions with NASA Swirl-Can Data (4) for Various Values of a Constant Mixing Intensity (solid curves); fixed primary zone parameters. . . . .	35 1/D2
12.	Comparison of NO <sub>x</sub> Predictions with NASA Swirl-Can Data (4) for Various Values of Mixing Intensity Decay Time (solid curves); fixed primary zone and initial intensity . . . . .	35 1/D2

FigurePage

13.	Comparison of NO <sub>x</sub> Predictions with NASA Swirl-Can Data (4) for Various Initial Mixing Intensity/Decay Time Pairs (solid curves); fixed primary zone and pair product . . . . .	40	1/D7
14.	Comparison of NO <sub>x</sub> Predictions with NASA Swirl-Can Data (4) using Parameter Values Fit at Different Inlet Temperatures (solid curves). . . . .	40	1/D7
15.	NO <sub>x</sub> Predictions versus Pressure for a NASA Swirl-Can Module, Baseline Case; see text for details; circles are test rig data obtained by NASA . . . . .	44	1/D11
16.	NO <sub>x</sub> Predictions versus Pressure for a NASA Swirl-Can Module, Parametric Study; see text for details middle curve of each trio is baseline case (Figure 15) . . . . .	47	1/D14
17.	NO <sub>x</sub> Predictions versus Initial Mixing Intensity for Various Values of Primary Zone Nonuniformity, Typical Engine Conditions; see text for details . . . . .	51	1/E4
18.	NO <sub>x</sub> Predictions versus Mixing Intensity Decay Time for Various Values of Primary Zone Nonuniformity, Typical Engine Conditions; see text for details. . . . .	51	1/E4
19.	NO <sub>x</sub> Predictions versus Primary Zone Volume for Various Values of Primary Zone Enrichment Factor, Typical Engine Conditions; see text for details . . . . .	52	1/E5
20.	NO <sub>x</sub> Predictions versus Primary Zone Nonuniformity for Various Values of Primary Zone Enrichment Factor, Typical Engine Conditions; see text for details. . . . .	54	1/E7
21.	Schematic of Boundary Conditions for Numerical Flow Calculations. . . . .	54	1/E7
22.	Streamline Plot of Calculated Flow Field; flow is from top to bottom, with symmetry axis at left side . . . . .	55	1/E8
23.	Diagram of Visualization Test Section flow is from top to bottom. . . . .	60	1/E13
24.	Helium-filled Soap Bubble Traces in Module Wake; mean flow is from top to bottom; bubbles are injected at tip of recirculation zone . . . . .	60	1/E13
25.	Streaklines of Water Droplets in Module Wake; flow is from right to left; water is injected behind swirler . . . . .	64	1/F3
26.	Closeup of Water Emerging from Swirler; water is injected behind swirler at center of hub. . . . .	64	1/F3
27.	Shadowgraph of Water Droplets in Module Wake; flow is from top to bottom; only left side of flow field is shown. . . . .	66	1/F5

28.	Combustion of Propane in Module Wake; overall equivalence ratio = 0.21; flow is from top to bottom, fuel is injected behind swirler . . . . .	68	1/F7
29.	Combustion of Pentane in Module Wake with Droplets Escaping; overall equivalence ratio = 0.41; flow is from top to bottom, fuel is injected behind swirler; droplets illuminated by strobe light. . . . .	68	1/F7
30.	Diagram of Test Section for Cold Flow Tracer Experiments; flow is from left to right . . . . .	69	1/F8
31.	Three Dimensional Plot of Tracer Concentrations at One Axial Station; axes at left define probed quadrant, distance along horizontal axis represents tracer concentration. . . . .	74	1/F13
32a.	Contour Map of Tracer Concentrations at 0.0045 Module Diameter Downstream; test section axis is at upper left, quadrant viewed looking upstream. . . . .	74	1/F13
32b.	Contour Map of Tracer Concentrations at 0.045 Module Diameter Downstream; test section axis is at upper left, quadrant viewed looking upstream. . . . .	75	1/F14
32c.	Contour Map of Tracer Concentration at 0.09 Module Diameter Downstream; test section axis is at upper left, quadrant viewed looking upstream. . . . .	75	1/F14
32d.	Contour Map of Tracer Concentrations at 0.18 Module Diameter Downstream; test section axis is at upper left, quadrant viewed looking upstream. . . . .	76	1/G1
32e.	Contour Map of Tracer Concentrations at 0.45 Module Diameter Downstream; test section axis is at upper left, quadrant viewed looking upstream. . . . .	76	1/G1
33.	Tracer Concentration versus Radius at Various Axial Stations; radius runs through swirler jet concentration peak at each station. . . . .	79	1/G4
34.	Diagram of Test Section and Probe for Gas Sampling under Burning Conditions; a modification of the cold flow tracer section (Figure 30); flow is from left to right. . . . .	79	1/G4
35a.	Contour Map of Equivalence Ratio at 0.22 Module Diameter Downstream; test section axis is at upper left, quadrant viewed looking upstream. . . . .	89	1/G14
35b.	Contour Map of Equivalence Ratio at 0.45 Module Diameter Downstream; test section axis is at upper left, quadrant viewed looking upstream. . . . .	89	1/G14



<u>Figure</u>		<u>Page</u>
35c.	Contour Map of Equivalence Ratio at 0.09 Module Diameter Downstream; test section axis is at upper left, quadrant viewed looking upstream. . . . .	90 2/A7
36a.	Contour Map of Nonuniformity Parameter at 0.22 Module Diameter Downstream; test section axis is at upper left, quadrant viewed looking upstream; values not meaningful in region of mottled shading. . . . .	90 2/A7
36b.	Contour Map of Nonuniformity Parameter at 0.45 Module Diameter Downstream; test section axis is at upper left, quadrant viewed looking upstream; values not meaningful in region of mottled shading. . . . .	91 2/A8
36c.	Contour Map of Nonuniformity Parameter at 0.9 Module Diameter Downstream; test section axis is at upper left, quadrant viewed looking upstream. . . . .	91 2/A8

# LIST OF TABLES

<u>Table</u>		<u>Page</u>	
1.	Rate Constants for the NO <sub>x</sub> Kinetic Reaction Scheme. . . . .	7	1/B2
2.	Typical Values for Quantities Entering into Rate Equation (11). . .	11	1/B6
3.	Inlet Temperatures and Pressures Appropriate to the NO <sub>x</sub> Time Constants and Formation Rates of Figures 2 through 6 . . . . .	14	1/B9
4.	Typical Data Appropriate to the Premixed NO <sub>x</sub> Calculations of Figure 7. . . . .	19	1/B14
5.	Data Relevant to a NO <sub>x</sub> Prediction Curve for the NASA Swirl-Can Combustor . . . . .	42	1/D9
6.	Fuel Droplet Evaporation Parameters and Calculated Results for Engine Conditions and a Simulation. . . . .	58	1/E11
7.	Measured and Predicted Droplet Sizes. . . . .	66	1/F5

NAS 1.26: 2977

**COMPLETED  
ORIGINAL**

# Nitric Oxide Formation in Gas Turbine Engines: A Theoretical and Experimental Study

Thomas Mikus, John B. Heywood,  
and R. Edward Hicks

GRANT NGR-22-009-378  
APRIL 1978

**NASA**

107

NASA Contractor Report 2977

Nitric Oxide Formation  
in Gas Turbine Engines:  
A Theoretical and Experimental Study

Thomas Mikus, John B. Heywood,  
and R. Edward Hicks  
*Massachusetts Institute of Technology  
Cambridge, Massachusetts*

Prepared for  
Lewis Research Center  
under Grant NGR-22-009-378



National Aeronautics  
and Space Administration

Scientific and Technical  
Information Office

1978

Blank  
Page



/

NITRIC OXIDE FORMATION IN GAS TURBINE ENGINES:  
A THEORETICAL AND EXPERIMENTAL STUDY

by Thomas Mikus<sup>\*</sup>, John B. Heywood, and R. Edward Hicks<sup>†</sup>

## 1. Introduction

The gas turbine engine is the dominant power plant in current aircraft. It has also achieved widespread use in industrial and utility applications. It even has the potential to achieve prominence as an engine for automobiles (1). In each of these categories, however, there is concern about the emission of oxides of nitrogen ( $\text{NO}_x$ ) from gas turbine engines. For example, in the case of aircraft turbines, the predicted growth in air traffic and the trend toward larger, higher pressure ratio engines are expected to greatly increase  $\text{NO}_x$  emissions in the vicinity of major airports. The Environmental Protection Agency has, as a consequence, proposed  $\text{NO}_x$  emission standards for aircraft gas turbine engines for January 1, 1979 (2). These standards will require about a factor of three reduction in emissions (in  $\text{lb}_m \text{NO}_2 / 1000 \text{ lb}_f \text{ thrust-hr}$ , averaged over a landing-take off cycle) from current jet engine levels.

It is well known that gas turbine  $\text{NO}_x$  emissions are most important at high engine power settings. Experimentally, it has been found that increases in combustor air inlet temperature and pressure, and thus engine compressor pressure ratio, increase  $\text{NO}_x$  emissions. For a given engine operating condition, the fuel injection technique, the air distribution, the combustor liner pressure drop and the residence time all affect  $\text{NO}_x$  emission levels.

---

<sup>\*</sup>Present address, Corporate Research Laboratory, Exxon Research & Engineering, Linden, New Jersey 07036.

<sup>†</sup>Present address, Chemical Engineering Research Group, Council for Scientific and Industrial Research, Pretoria 0001, South Africa.

The oxides of nitrogen which leave the engine are almost all nitric oxide, NO, with only a few percent nitrogen dioxide, NO<sub>2</sub>. It has been shown that the engine exhaust NO concentration depends on rate-limited reactions occurring in the burning gases in the high temperature zones of the combustor. As additional air is mixed with the combustion products to cool the gases before entry to the turbine, the NO formation chemistry freezes. After this point, the NO concentration only changes due to dilution.

In attempts to achieve required reductions in NO<sub>x</sub> emissions, several new combustor concepts are being developed. A computer program which models the NO<sub>x</sub> formation process in gas turbine combustors is described herein. The model was developed to assist in optimizing the design of combustors. It can be used to extrapolate test data from a combustor on a test stand to actual engine operating conditions. It can also assist in identifying key design parameters which have the greatest effect on NO<sub>x</sub> emissions.

This type of model has been used extensively to predict NO<sub>x</sub> emissions from conventional combustors. The results of these studies have been reviewed recently by Heywood and Mikus (3), and it was shown that relatively simple models which include only the major parameters affecting NO formation can be used to predict NO<sub>x</sub> emissions.

The design goals of a number of advanced combustors now being developed for low NO<sub>x</sub> emissions can be summarized as follows. The intent is to create a primary combustion zone within the combustor

which is fuel lean, where the fuel and air are well mixed together, with as short a residence time in the high temperature zone as is consistent with the required combustion efficiency. These characteristics, for a given engine operating condition, promise minimum  $\text{NO}_x$  emissions.

One of the advanced combustor concepts, the NASA swirl-can modular combustor (4), is built upon the use of discrete modules whose characteristic size is small compared to overall combustor dimension (5 cm compared to 100 cm). A recirculating wake is produced downstream of each module which can be made lean and intensely mixed; its size is similar to the module's characteristic size. This is how the design goals mentioned in the previous paragraph are approached.

The scope of this report is to develop a calculational model for the formation of  $\text{NO}_x$  in gas turbine engines. This model is general in nature and should be applicable to a range of combustor concepts and combustor geometries; however, the examples and discussions are generally directed toward aircraft applications. Emphasis is placed on the application of this model to the NASA swirl-can modular combustor, and comparisons of modeling prediction with experimental  $\text{NO}_x$  data are now available. The report also makes immediate use of predictions generated by this  $\text{NO}_x$  model. Experimental data are obtained to support assumptions and parameter values used in the model, so that the modeling predictions may be used with some confidence.

The next section describes the particulars of the  $\text{NO}_x$  model, including the "building blocks" which can be assembled to generate  $\text{NO}_x$  predictions for a wide variety of combustors. The third section assembles these blocks and compares the resulting predictions with available  $\text{NO}_x$  data

for different combustors, noting the influence of the modeling parameters. Section 4 is an analysis of Section 3's predictions relevant to the NASA swirl-can combustor, demonstrating that much can be learned about a combustor's operation simply by matching its  $\text{NO}_x$  emissions data. The fifth section describes parametric modeling studies which provide examples of the further usefulness of the  $\text{NO}_x$  model in extrapolating test data and in designing for low  $\text{NO}_x$ ; further insight is also obtained into the influence of the modeling parameters.

Sections 6 through 10 are directed toward the verification of the assumptions and parameter values which went into the  $\text{NO}_x$  modeling of the NASA swirl-can combustor. The sixth section presents a calculation of the streamlines downstream of a module in order to get an overall view of the flow in this combustor. Section 7 describes calculations of the fuel droplet formation and evaporation processes which occur within that flow field. Flow visualization experiments which document the turbulent recirculation and fuel droplet processes downstream of the module are exhibited in Section 8. The ninth section is a presentation of non-burning tracer experiments which quantitatively follow the streamlines from the swirler jets downstream, as they entrain adjacent gases. Experiments conducted under burning conditions are presented in Section 10; they map out the flow field in terms of both local equivalence ratio and local nonuniformity. A summary and conclusions are set forth in the final section.

## 2. Model Description

### 2.1 Chemical kinetics of NO<sub>x</sub> formation

At the temperatures, pressures, and equivalence ratios found in gas turbine combustors, NO formation may be calculated from the set of six chemical reactions used by Lavoie et al (5). The three most important reactions are a modification of the Zeldovich mechanism:



Reactions involving N<sub>2</sub>O as an intermediary may become important at temperatures below 2100 K, especially if concentrations are substantially greater than equilibrium values. Three such reactions which were included in the calculational scheme are:



A reaction cited by LeTrung et al (6) which came under consideration too late to be used in many of the calculations is:





For typical conditions of interest the above reaction is more important than reactions (4) and (5), but as will be shown below, all of the  $N_2O$  reactions may generally be neglected with little effect on the  $NO_x$  formation rate. Rate constants taken from Baulch et al. (7) are presented in Table 1.

The reaction scheme may be written as rate equations for  $NO$ ,  $N$ , and  $N_2O$  (if included), but first the method for calculating the concentrations of  $O$ ,  $O_2$ ,  $OH$ , and  $H$  must be resolved. The  $N_2$  concentration is essentially constant. The appropriate assumptions depend on the pressure, temperature and atomic composition of the system being analyzed. These assumptions should be suitable for typical gas turbine combustor conditions, i.e., pressures  $\approx 5$ -30 atm, peak temperatures  $\approx 2500$  K, residence times at these peak conditions  $\approx 1$ -3 msec, equivalence ratio for hydrocarbon-air combustion between about 0.6 and 1.3.

A model for the flame front in the combustor must be formalized before appropriate assumptions can be made. Heywood (8) and Westenberg (9) have justified the assumption that under appropriate conditions, the  $O$ ,  $O_2$ ,  $OH$  and  $H$  concentrations are the equilibrium values. The argument can be summarized as follows.

In a premixed one-dimensional flame, there is a thin initial reaction zone where radicals are generated and react with the hydrocarbon fuel. Most of the temperature rise occurs in this zone. This region is followed by a thicker zone where  $CO$  is oxidized to  $CO_2$ , and

TABLE 1

Rate Constants for the  $\text{NO}_x$  Kinetic Reaction Scheme

Reaction, i	Rate const., $k_i$ , $\text{cm}^3\text{gmole}^{-1}\text{sec}^{-1}$
1	$7.6 \times 10^{13} \exp(-38,000/T)$
2	$1.5 \times 10^5 T \exp(-19,500/T)$
3	$4.1 \times 10^{13}$
4	$7.6 \times 10^{13} \exp(-7,600/T)$
5	$6.3 \times 10^{13} \exp(-55,200/T)$
6	$1.3 \times 10^{12} \exp(-32,100/T)$
7*	$5.0 \times 10^{14} \exp(-29,000/T)$

where T is temperature in K

---

\* for M = A; no recommendation for M =  $\text{N}_2$

radicals present in greater than equilibrium concentrations recombine through trimolecular reactions. If the NO formed in this non-equilibrium region is much less than the amount formed downstream of the flame, then the O, O<sub>2</sub>, OH, and H equilibrium assumption is a reasonable approximation. There have recently been studies of CO equilibration in the flame zone at pressures, temperatures and equivalence ratios typical of a combustor primary zone (10). These studies show that equilibration times are less than  $2 \times 10^{-4}$  sec (for equivalence ratios between 0.6 and 1.3) which is much less than typical primary zone residence times, and that the effect of radical concentrations above equilibrium values within the hydrocarbon reaction zone will not significantly increase NO emissions. The amount of NO formed in the reaction zone of the flame is small compared with the amount formed downstream of the flame at gas turbine combustor conditions.

Following Lavoie et al (5) and assuming equilibrium concentrations for N<sub>2</sub>O, O<sub>2</sub>, OH, and H, the rate equations for NO, N, and N<sub>2</sub>O can be written as

$$\rho \frac{d}{dt} \frac{[NO]}{\rho} = -\alpha (BR_1 + R_2 + R_3 + 2\alpha R_6) + R_1 + \beta (R_2 + R_3) + 2\gamma R_6 \quad (8)$$

$$\rho \frac{d}{dt} \frac{[N]}{\rho} = -\beta (\alpha R_1 + R_2 + R_3) + R_1 + \alpha (R_2 + R_3) \quad (9)$$

$$\rho \frac{d}{dt} \frac{[N_2O]}{\rho} = -\gamma (R_4 + R_5 + R_6 + R_7) + R_4 + R_5 + \alpha^2 R_6 + R_7 \quad (10)$$

where  $\rho$  is the gas density;  $\alpha = [\text{NO}]/[\text{NO}]_e$ ,  $\beta = [\text{N}]/[\text{N}]_e$ , and  $\gamma = [\text{N}_2\text{O}]/[\text{N}_2\text{O}]_e$  are, respectively, the concentrations of NO, N, and  $\text{N}_2\text{O}$  divided by their equilibrium concentrations; and  $R_i$  is the "one-way" equilibrium rate of the  $i$ th reaction, e.g.,  $R_1 = k_1[\text{N}_2]_e[\text{O}]_e$ . Rough estimates of the magnitude of the terms in these equations indicate that the relaxation times for the  $[\text{N}]$  and  $[\text{N}_2\text{O}]$  equations are several orders of magnitude shorter than that for the  $[\text{NO}]$  equation. It is therefore an excellent approximation to assume steady-state concentrations for N and  $\text{N}_2\text{O}$  and set  $d([\text{N}]/\rho)/dt$  and  $d([\text{N}_2\text{O}]/\rho)/dt = 0$ . Equations (9) and (10) can then be used to eliminate  $\beta$  and  $\gamma$  from equation (8); rearranging in terms of the mass fraction of nitric oxide,  $\{\text{NO}\}$ , the rate equation becomes

$$\frac{d\{\text{NO}\}}{dt} = \frac{M_{\text{NO}}}{\rho} (1-\alpha^2) \left( \frac{R_1}{1+\alpha K_1} + \frac{R_6}{1+K_2} \right) \quad (11)$$

Where  $\{\text{NO}\}$  is the mass fraction of NO,  $M_{\text{NO}}$  is the molecular weight of NO,  $K_1 = R_1/(R_2 + R_3)$  and  $K_2 = R_6/(R_4 + R_5 + R_7)$ . The first term in the large bracket on the right-hand side of the above equation is the result of reactions (1)-(3), the extended Zeldovich chain mechanism. The second term is the result of reactions (4)-(7) and involves  $\text{N}_2\text{O}$  as an intermediary. In general,  $K_1$ ,  $K_2$ , and  $\alpha$  are of order unity or less, and the relative importance of the two mechanisms just described is determined by the ratio of  $R_1$  to  $R_6$ . This is much larger than unity except at low temperatures (less than 2100 K).

Typical values for the quantities found in equation (11) are given in Table 2. Many of the calculations presented herein have been made with  $R_7=0$ ; however, reactions (4)-(7) usually contribute relatively little to  $\text{NO}_x$  formation, as can be seen from an examination of equation (11) in light of the values presented in Table 2. For a local mixture richer than  $\phi \gtrsim 0.7$ , the  $R_6$  term is much smaller than the  $R_1$  term, barring rare situations where NO is far above equilibrium levels ( $\alpha \gg 1$ ). For a local mixture leaner than  $\phi \lesssim 0.6$ , the  $R_6$  term becomes comparable to the  $R_1$  term, but both are insignificant relative to richer mixtures. In addition, for mixtures which are too lean, the kinetic scheme is invalid due to the combustion reaction time constants becoming comparable to the residence time. Thus, except for cases where essentially all (on a molecular scale) of the burned gases are quite lean, equation (11) may be simplified to

$$\frac{d\{\text{NO}\}}{dt} \approx \frac{2M_{\text{NO}}R_1(1-\alpha^2)}{\rho(1+\alpha K_1)} \quad (12)$$

Equations (11) and (12) show that the NO formation rate depends only on the pressure, temperature, atomic composition and NO concentration downstream of the thin flame zone. NO profiles calculated with equation (11) as a function of time downstream of a one-dimensional flame for a stoichiometric mixture are shown in Fig. 1. Since primary zone residence times are of order or less than 3 msec and peak temperatures  $\sim 2500$  K, one would not expect NO concentrations to reach equilibrium levels within the high temperature zone of a gas turbine combustor.

This argument can be made more precise. For  $\alpha \ll 1$ , equation (11) can be rearranged as



TABLE 2

Typical Values for Quantities Entering into Rate Equation (11) for NO

inlet air temperature	590 K	
pressure	5.8 atm	
fuel	kerosene	
$M_{\text{NO}}$	30 g gmole <sup>-1</sup>	
equivalence ratio	0.8	0.5
burned gas temperature, K	2250	1730
$\rho$ , g cm <sup>-3</sup>	$9.1 \times 10^{-4}$	$1.2 \times 10^{-3}$
$R_1$ , gmole cm <sup>-3</sup> sec <sup>-1</sup>	$7.5 \times 10^{-7}$	$2.3 \times 10^{-10}$
$K_1$	0.41	0.20
$R_6$ , gmole cm <sup>-3</sup> sec <sup>-1</sup>	$3.0 \times 10^{-8}$	$1.1 \times 10^{-10}$
$K_2$	0.029	0.008
$K_2$ for $R_7 = 0$	0.21	0.63
$\left. \frac{d(\text{NO})}{dt} \right _{\alpha=0}$ , sec <sup>-1</sup>	$5.1 \times 10^{-2}$	$1.7 \times 10^{-5}$

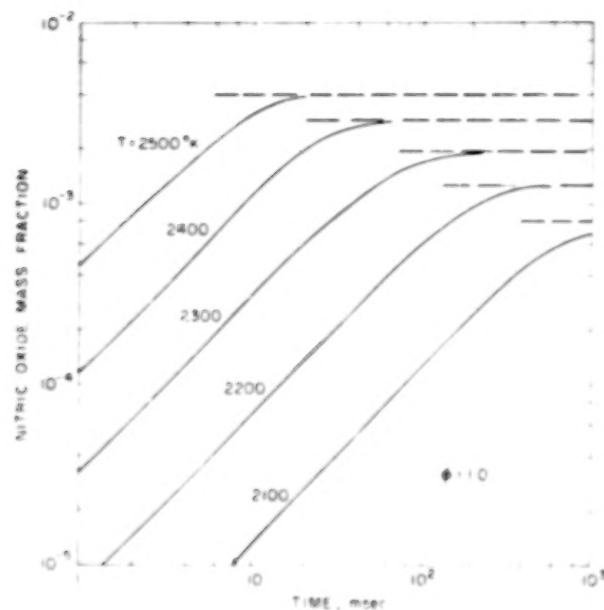


Figure 1. NO versus Time for Stoichiometric Burned Gas at Various Temperatures; pressure=15 atm; fuel=kerosene; dashed lines are equilibrium levels from Heywood, *et al.* (11)

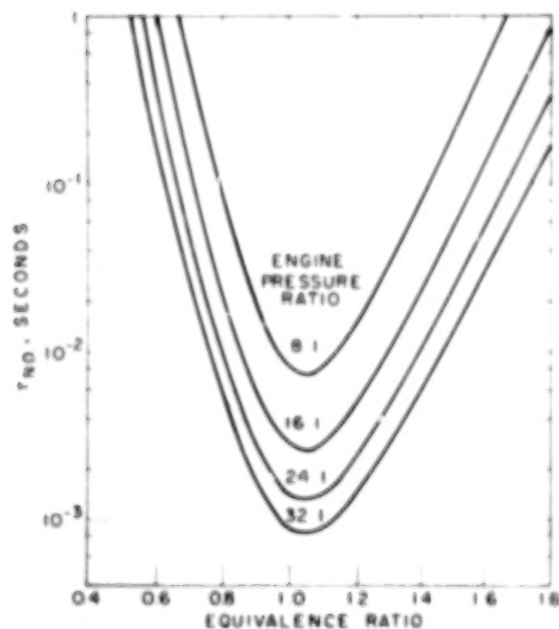


Figure 2. Characteristic Time for NO formation versus Equivalence Ratio for Various Engine Pressure Ratios; see Table 3 for inlet conditions.

$$\frac{1}{\{NO\}_e} \frac{d\{NO\}}{dt} = \frac{2M_{NO}}{\rho\{NO\}_e} (R_1 + \frac{R_6}{1 + K_2}) = \frac{1}{\tau_{NO}} \quad (13)$$

$\{NO\}_e^{-1} d\{NO\}/dt$  has the units  $\text{sec}^{-1}$  and can be thought of as the reciprocal of the characteristic time,  $\tau_{NO}$ , of the NO formation chemistry.

Generally, this equation may be simplified to

$$\frac{1}{\{NO\}_e} \frac{d\{NO\}}{dt} \approx \frac{2M_{NO} R_1}{\rho\{NO\}_e} \approx \frac{1}{\tau_{NO}} \quad (14)$$

as was argued for equation (12).

Since the gas turbine combustor is essentially adiabatic, the burned gas temperature and concentrations of major species are determined by the combustor inlet air conditions, local equivalence ratio, and fuel properties. In a simple-cycle gas turbine engine, combustor inlet conditions are determined by engine inlet conditions, compressor pressure ratio and efficiency, and pressure losses. Values of  $\tau_{NO}$  from equation (13) are plotted in Fig. 2 as a function of equivalence ratio for different engine compressor pressure ratios, assuming 1 atm., 288 K inlet air, 90% polytropic compressor efficiency, and 5% total pressure loss across the combustor liner (see Table 3).

The kinetic scheme for NO formation presented in this subsection will be tested in Subsection 3.1.

## 2.2 Effects of fuel-air nonuniformities; a primary zone model

To apply the above NO kinetic scheme to a heterogeneous combustion zone, this description of a premixed one-dimensional flame must now be

TABLE 3

Inlet Temperatures and Pressures Appropriate to the  $\text{NO}_x$  Time Constants  
and Formation Rates of Figures 2 through 6

Compressor Pressure Ratio	Combustor Inlet Air Temp, K ( $^{\circ}\text{F}$ )	Combustor Pressure atm (psia)
8:1	555 (538)	7.6 (112)
16:1	685 (774)	15.2 (223)
24:1	772 (933)	22.8 (335)
32:1	840 (1052)	30.4 (447)

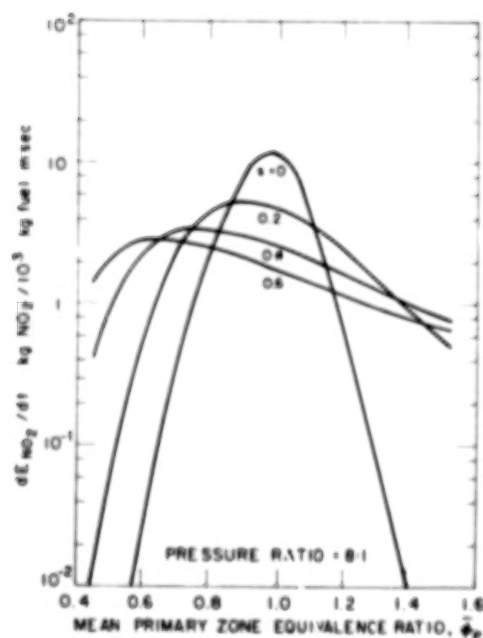


Figure 3. Rate of Increase in  $\text{NO}_x$  Emission Index versus Mean Equivalence Ratio for Various Values of Nonuniformity Parameter, 8:1 Engine Pressure Ratio; see Table 3 for inlet conditions.

related to the flame structure in a gas turbine combustor. Fuel as a liquid spray and air enter the primary zone separately in approximately stoichiometric proportions. The fuel droplets vaporize as they move relative to the primary zone gases leaving wakes rich in fuel vapor, which then mix with air and already burned gas, and burn. Mixing of fuel and air to a uniform equivalence ratio would not be expected. As the fuel droplets vaporize, fuel vapor and air mix and form turbulent "eddies" or pockets of combustible mixture with a wide range of fuel-air ratios.

High speed movies of liquid-fueled combustors and burners suggest that the thin flame front model described in Subsection 2.1 is still applicable. In such combustors low luminosity blue flame fronts propagate through some of the fuel/air eddies, while soot-forming, luminous, yellow flame fronts envelope and consume other fuel/air eddies. Such an unsteady turbulent flame structure would be expected in the vigorously stirred primary zone where fuel and air enter separately. As a consequence, burned gas eddies are produced with a distribution in fuel-air ratio about the mean primary zone value. This distribution will change with time as these eddies mix with each other, and with dilution air, through the action of turbulence and molecular diffusion.

Details of the fuel introduction method and air flow pattern determine the initial droplet size and spatial distribution. The air flow pattern further dictates the process of droplet motion and evaporation as well as the subsequent mixing intensity. Thus, fuel introduction and air flow affect both the initial spread of the burned gas fuel-air ratio distribution and its change with time. This physical description of the combustion process is the basis for the model which will now be described.



The importance of nonuniformities can be illustrated as follows. Since fuel and air are not uniformly mixed, different burned gas eddies will have different average fuel fractions during their residence time in the combustor primary zone. The use of fuel fraction  $F$  (fuel mass divided by total mass) in a mass-based distribution function simplifies the mathematics, compared to using fuel-air ratio or equivalence ratio. Assuming a Gaussian distribution function for fuel fraction about the mean fuel fraction  $\bar{F}$ ,

$$f(F) = (1/2\pi\sigma^2)^{1/2} \exp\{-(F - \bar{F})^2/2\sigma^2\} \quad (15)$$

then the fraction (by mass) of the burned gas flow with fuel fraction between  $F$  and  $F + dF$  is  $f(F) dF$ .  $\sigma$  is the standard deviation of the distribution and a mixing parameter

$$s = \sigma/\bar{F} \quad (16)$$

can be used as a measure of nonuniformity.

Figures 3 through 6 show the effect of nonuniformities on NO formation rates (plotted as  $dE_{NO_2}/dt$ ) for four different engine compressor pressure ratios;  $E_{NO_2}$  is a global emission index expressing oxides of nitrogen as equivalent kg  $NO_2$  per 1000 kg of fuel burned. The simplifying assumption has been made that NO is far below equilibrium ( $\alpha \ll 1$ ). Equation (11) has been used to calculate the perfectly mixed case ( $s = 0$ ). For nonuniform mixtures ( $s > 0$ ) values of  $dE_{NO_2}/dt$  obtained from equation (11) for a range of  $\phi$  are weighted by equation

(15) to determine an average NO formation rate at each average equivalence ratio. For stoichiometric mixtures, the mean NO formation rate is substantially reduced as the primary zone becomes less uniform. For rich ( $\bar{\phi}_p > 1.2$ ) and lean ( $\bar{\phi}_p < 0.7$ ) the mean NO formation rate is substantially increased. It has been shown that values of  $s$  between 0.3 and 0.7 are required to match predicted  $\text{NO}_x$  emissions to measurements in conventional combustors<sup>(3)</sup>.

Approximate estimates of combustor  $\text{NO}_x$  emissions can be made using Figures 3 through 6. For example, Figure 5 is appropriate for combustors used in state-of-the art engines in the 40,000 + lb<sub>f</sub> thrust class at take-off conditions. Assuming an  $s = 0.4$  is typical for the combustor,  $dE_{\text{NO}_2}/dt$  is almost constant between  $0.6 < \bar{\phi}_p < 1.0$ . Assuming a residence time for the burned gas within this equivalence ratio range of 1 to 2 msec, and an average value for  $dE_{\text{NO}_2}/dt$  of 24 kg  $\text{NO}_2/1000$  kg fuel msec, gives an  $E_{\text{NO}_2}$  between 24 and 48 kg  $\text{NO}_2/1000$  kg fuel. This spans the measured range of 30-40 kg  $\text{NO}_2/1000$  kg fuel.

These graphs also indicate desirable combustor operating conditions for low  $\text{NO}_x$  emissions.  $dE_{\text{NO}_2}/dt$  decreases below levels found in conventional combustors only for  $\bar{\phi}_p < 0.7$ , and then only if the uniformity of the fuel-air mixture is significantly improved. Thus a lean, well mixed, short residence time primary combustion zone is required, with the most significant gains coming from better fuel-air mixing.

For detailed  $\text{NO}_x$  calculations a primary zone treatment has been implemented using the approaches set forth in this subsection. The primary zone is modeled as a partially stirred (or macro-mixed) reactor. It is assumed that the fuel and air which enter the primary zone are

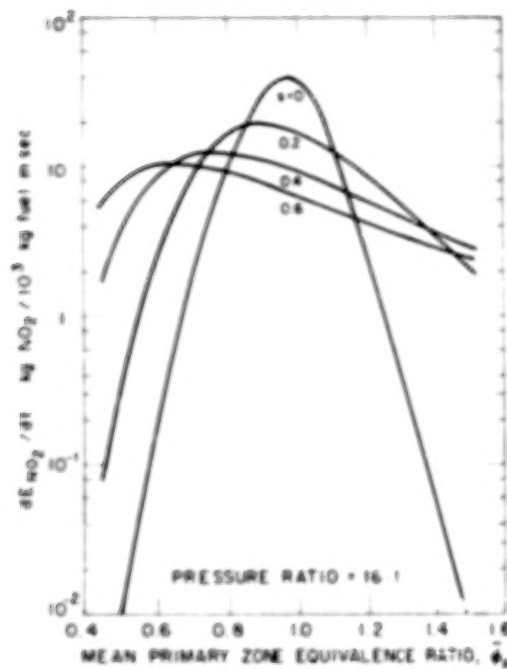


Figure 4. Rate of Increase in  $\text{NO}_x$  Emission Index versus Mean Equivalence Ratio for Various Values of Nonuniformity Parameter, 16:1 Engine Pressure Ratio; see Table 3 for inlet conditions.

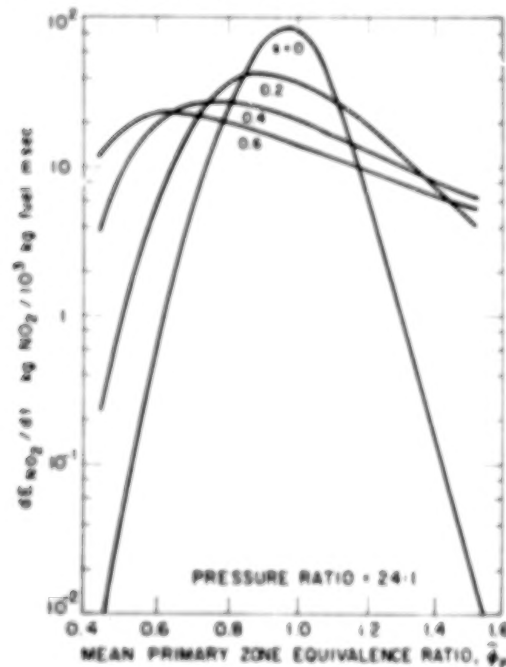


Figure 5. Rate of Increase in  $\text{NO}_x$  Emission Index versus Mean Equivalence Ratio for Various Values of Nonuniformity Parameter, 24:1 Engine Pressure Ratio; see Table 3 for inlet conditions.

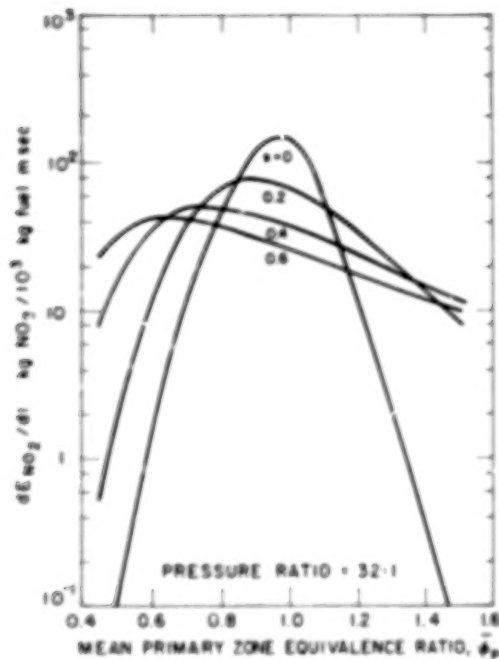


Figure 6. Rate of Increase in  $\text{NO}_x$  Emission Index versus Mean Equivalence Ratio for Various Values of Nonuniformity Parameter, 32:1 Engine Pressure Ratio; note  $\text{NO}_x$  scale shift from previous figures; see Table 3 for inlet conditions.

TABLE 4

Typical Data Appropriate to the Premixed  $\text{NO}_x$  Calculations of Figure 7

unburned mixture temperature	800 K	
pressure	5.5 atm	
fuel	propane	
equivalence ratio	0.7	1.0
burned gas temperature	2380 K	2670 K
residence time	3.6 msec	3.1 msec

rapidly dispersed throughout the zone to form discrete fluid eddies of a scale small compared with combustor dimensions.

For a stirred reactor, the fraction (by mass) of the flow with residence time between  $t$  and  $t + dt$  is  $\psi(t)dt$  where:

$$\psi(t) = (1/\tau_p) \exp(-t/\tau_p) \quad (17)$$

$\tau_p$  is the mean residence time for the primary zone, which can be calculated as

$$\tau_p = \frac{V_p}{\dot{m}_p \bar{v}} \quad (18)$$

where  $V_p$  is the primary zone volume,  $\dot{m}_p$  is the mass flow rate through the zone, and  $\bar{v}$  is the mean specific volume within the zone. Since all of the fuel must pass through the primary zone,

$$\dot{m}_p = \frac{\dot{m}_o F_o}{F_p} \quad (19)$$

where  $\dot{m}_o$  is the overall combustor mass flow and  $F_p/F_o$  is the ratio of primary zone to overall fuel fraction. By definition

$$\bar{v} = \int_0^1 v(F) f(F) dF \quad (20)$$

where  $f(F)$  comes from substituting  $\bar{F} = F_p$  and  $s = s_p$ , the primary zone nonuniformity parameter, into equations (16) and (15). Thus, three

parameters are required to model the primary zone.  $V_p$ ,  $F_p/F_o$  and  $s_p$  were chosen because they are expected to be weak functions of combustor operating conditions.

$NO_x$  predictions for the primary zone are then calculated as

$$\{NO\}_p = \int_0^1 \int_0^\infty \{NO\}(F,t) \psi(t) dt f(F) dF \quad (21)$$

where  $\{NO\}(F,t)$  is obtained by integrating equation (11) starting from  $\{NO\} = 0$  at  $t = 0$ .  $\{NO\}$  might also be started from a level which approximated "flame-front NO", but this level is negligible for the cases presented herein. The integral on  $t$  has been derived semi-analytically. The integral on  $F$  is performed by creating a statistical ensemble of equal mass "fluid elements" whose fuel fractions represent  $f(F)$ , and then averaging over these elements.

### 2.3 A multi-zone flow model with Monte Carlo mixing

In general,  $NO_x$  production is not confined to the primary zone. Further downstream where additional air is added, it is necessary to model one or more zones where mixing processes are proceeding concurrently with  $NO_x$  formation. A statistical method of following a chemical reaction (such as nitric oxide formation) through the course of a mixing process was described by Corrsin<sup>(12)</sup>, and has been adapted more recently by Flagan and Appleton<sup>(13)</sup>.

With this method the flow through a zone is represented by a statistical ensemble of fluid elements of equal mass. At any point in time each element has its own local fuel fraction. The number of

elements should be large enough to fairly characterize the distribution of fuel fractions. This number was between 250 and 1000 for the calculations presented herein. The ensemble of fluid elements experiences mixing interactions which represent the dilution and mixing process. These interactions occur at time intervals of

$$\Delta t = 1/\beta N \quad (22)$$

where  $\beta$  is the current value of the mixing intensity and  $N$  is the total number of fluid elements in the statistical ensemble. Each mixing interaction is calculated as follows: (i) Two different fluid elements are chosen at random. (ii) For each fluid element the nitric oxide formation parameters corresponding to its local fuel fraction are obtained by interpolation from a table of parameters appropriate to the combustor inlet air pressure and temperature and the fuel properties. These parameters are the specific volume of the burnt gases,  $v$ , and a set of parameters required for the use of equation (11). (iii) Starting with the nitric oxide mass fraction each element contained immediately after its previous interaction, equation (11) is integrated semi-analytically up to the current time. If this is an element's first interaction, the integration starts with the nitric oxide mass fraction contained when it entered the zone. (iv) These integrated nitric oxide mass fractions are averaged to represent complete mixing of the two interacting elements. (v) Both elements are assigned a new fuel fraction equal to the average of the two prior to mixing.

For each time increment there is a corresponding volume increment

which represents the progress of the flow through the zone's volume

$$\Delta V = \dot{m} \Delta t \bar{v} \quad (23)$$

where  $\dot{m}$  is the zone's mass flow rate and  $\bar{v}$  is the current average specific volume. When the entire zone volume has been swept out by these incremental volume flows, the local nitric oxide mass fractions for all of the fluid elements are updated and averaged. This average represents the mean nitric oxide mass fraction at the zone's exit.

Within the framework of this model is the freedom to specify the mixing intensity  $\beta$  as a function of time. This will be utilized in the modeling calculations presented in Subsection 3.2.

The dilution zone model is easily linked into a computation. If the preceding zone is a primary zone model as described in Subsection 2.2, there will be an ensemble of fluid elements corresponding to the flow which passes through the primary zone. Each element has its own local fuel fraction and current nitric oxide mass fraction. To form the ensemble of fluid elements for the dilution zone is simply a matter of taking the primary zone ensemble and adding a number of new elements which corresponds to the mass flow rate of additional air which is entering the dilution zone. These new elements will of course have fuel fractions and nitric oxide mass fractions equal to zero, since they represent pure air.



### 3. Comparisons of $\text{NO}_x$ Predictions with Available Experimental Data

#### 3.1 A "premixed" tubular burner

The kinetic scheme for nitric oxide formation described in Subsection 2.1 is best tested by comparing predicted  $\text{NO}_x$  levels with measurements from a premixed burner. The fuel and air should be completely premixed ( $s=0$ ), and the flow should be adiabatic, with a well-defined residence time - a one-dimensional flow system, for example. Anderson (14,15) presented  $\text{NO}_x$  measurements from a burner which approached these requirements. It was a tubular burner 4 inches in diameter, consisting of a propane injector/mixer, 20 to 25 diameters of mixing region, a plate with cylindrical passages for flameholding and up to 4.5 diameters of reaction zone; a cooled gas sample probe was located on the axis of the burner.

For this geometry a plug flow assumption should be quite accurate. The radiative heat transfer from the burner centerline was estimated, and found to decrease the burned gas temperature by less than 15 K; therefore, the gas flowing along the centerline was assumed to be adiabatic. The triangles in Figure 7 are the  $\text{NO}_x$  emission index data at various equivalence ratios presented by Anderson (15), measured 30 cm downstream of the flameholder, for the case of 5.5 atm, 800 K inlet mixture temperature, and 25 m/sec reference velocity. The curve labeled A shows the  $\text{NO}_x$  model predictions for the completely uniform case; some data relevant to these predictions are given in Table 4. Curve A is generally in good agreement with the data over a wide range of emission index, especially in the main region of interest

$10 < E_{\text{NO}_2} < 40$ . The  $\text{NO}_x$  predictions are not expected to be accurate at equivalence ratios lower than about 0.5, where temperatures are lower than 2100 K (see Subsection 2.1). At equivalence ratios near unity Anderson states that his data may be in error due to catalytic reduction of NO in his stainless steel probe; this would explain some of the discrepancy between predictions and data at the higher equivalence ratios.

As seen in Subsection 2.2, a less peaked prediction curve may be generated by assuming a certain degree of nonuniformity ( $s > 0$ ). Curve B of Figure 7 shows  $\text{NO}_x$  predictions for  $s = 0.1$ . This curve follows the general trend of Anderson's data significantly better than curve A. It should be noted that these data were obtained downstream of a water-cooled flameholder, which would lower burned gas temperatures; the predictions assume adiabatic conditions. If curve B were corrected for heat transfer to the flameholder, it would agree with the data even more closely.

Figure 8 presents comparisons for lower inlet mixture temperatures. The triangles in this figure are again data from Anderson (15); conditions were the same as for the data of Figure 7, except that the inlet mixture temperature was 600 K. The solid curve labeled A again shows  $\text{NO}_x$  model predictions for the completely uniform case, while solid curve B is for  $s = 0.15$ . The agreement between the predictions and the data is not as good as for the higher inlet mixture temperature case, but as in Figure 7 agreement is better for the nonuniform predictions. Burned gas temperatures will

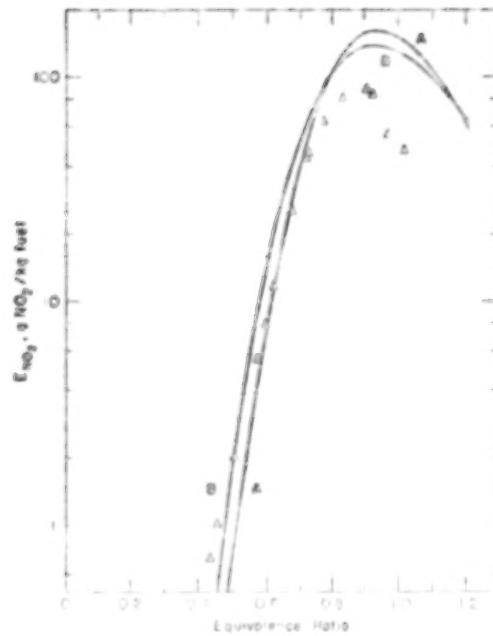


Figure 7. Comparison of  $\text{NO}_x$  Predictions with Premixed Experimental Data,  $800^\circ\text{K}$  Inlet; pressure = 5.5 atm;  $s = 0$  for curve A,  $s = 0.1$  for curve B; data from Anderson (15).

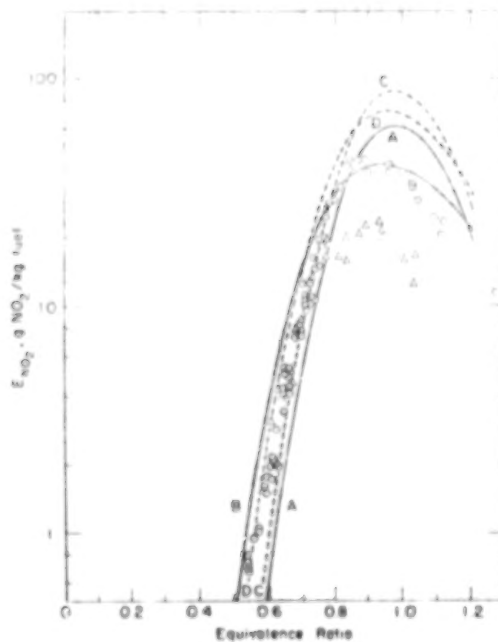


Figure 8. Comparison of  $\text{NO}_x$  Predictions with Premixed Experimental Data,  $600^\circ\text{K}$  Inlet; see text for details.

be below 2100 K for equivalence ratios less than about 0.6 in this case, so that  $\text{NO}_x$  predictions are not expected to be accurate in that range. As in Figure 7, catalysis in the sample probe may have depressed the  $\text{NO}_x$  data at the richer equivalence ratios, and a flameholder heat transfer correction would lower the predictions; these factors would improve the agreement.

The circles in Figure 8 are data from an earlier Anderson paper (14). These data were measured 46 cm downstream of the flameholder, for the case of 5.5 atm, 590 K inlet mixture temperature, and 23 m/sec reference velocity, roughly comparable to the other data in Figure 8. However, the data circles were obtained with a different propane injector/mixer design, and an uncooled flameholder only one-third as thick. The dashed curves labeled C and D are the  $\text{NO}_x$  emission predictions for  $s=0$  and  $s=0.1$ , respectively. These predictions follow the data quite nicely up to an equivalence ratio of about 0.85; above this level there is some discrepancy. Sample probe catalytic effects could explain some of this. Generally, this set of data seems more uniform, i.e. is better matched by  $\text{NO}_x$  predictions with a low  $s$  value, probably due to differences in the propane injector/mixer. Also, heat transfer to the flameholder would be less significant than for the other data, so that the  $\text{NO}_x$  predictions need not be adjusted downward.

There are two conclusions which may be drawn from a comparison of the predictions and data presented in Figures 7 and 8. (1) The nitric oxide kinetic scheme agrees reasonably well with measurements

from a simple burner. (ii) Although it was much more uniform than state-of-the-art gas turbine combustors, the "premixed" burner described above probably did not produce a completely uniform fuel-air mixture.

For a stoichiometric mixture, a calculation of the average mixing intensity required to produce a nonuniformity of  $s=0.15$  at the flameholder (starting from pure fuel and air at the fuel injector) yields the value  $\beta=70 \text{ sec}^{-1}$ . Compare this number with a value of approximately  $20 \text{ sec}^{-1}$  for pipe-flow turbulence under these conditions. The additional mixing could easily be accounted for by considering the initial mixing produced by the propane injector/mixer. Thus, the fuel-air mixture in this burner should not be expected to be completely uniform.

### 3.2 The NASA swirl-can modular combustor

A more complete evaluation of the  $\text{NO}_x$  model described in Section 2 requires the examination of a combustor with a flow field more complicated than the burner described in the previous subsection. The NASA modular swirl can combustor is an unconventional annular design (4). Fuel is introduced into 120 swirl cans arranged in three concentric rings at the same axial station. Most of the air flows through these modules and in between them at the plane of the "blockage plates" which are the maximum axial cross-sections of the swirl cans. Only about 6% of the total air flow is used as liner cooling air and does not pass through or between the swirl cans.

Figure 9 shows the construction of a swirl can. Air flows from the left, entering the can and mixing with fuel, which is sprayed onto the swirler plate from a fuel tube inside the can. The fuel-air mixture passes through the swirler and burns in the wake of the module. Some of the air which has passed around the module is entrained into the recirculating wake flow. Cold-flow tests confirm that this recirculating wake extends approximately one blockage-plate diameter downstream. The air which flows around the module but is not entrained into this "primary zone" will mix with the combustion products from the primary zone further downstream. Figure 10 is a tangential view of the combustor showing the swirl can modules mounted at the entrance plane of the annular liner.

At low fuel-air ratios the combustion occurs within small primary zones in the wake of each swirl can. As the overall fuel-air ratio approaches stoichiometric (0.069), the primary zones coalesce into a single "ring of fire." These two extremes of fuel-air ratio serve as limiting cases which are the bases for the first two sets of  $\text{NO}_x$  predictions described in this subsection. These limiting cases allow the  $\text{NO}_x$  calculation to be made with a single "primary" zone as described in Subsection 2.2. Later in this subsection the dilution zone presented in Subsection 2.3 will be added to make a more complete model of  $\text{NO}_x$  formation in this NASA combustor.

In the limit of low fuel-air ratios, so little fuel is being added to the flow through the swirl cans that combustion in the module wakes occurs at fuel-lean conditions. Any subsequent mixing

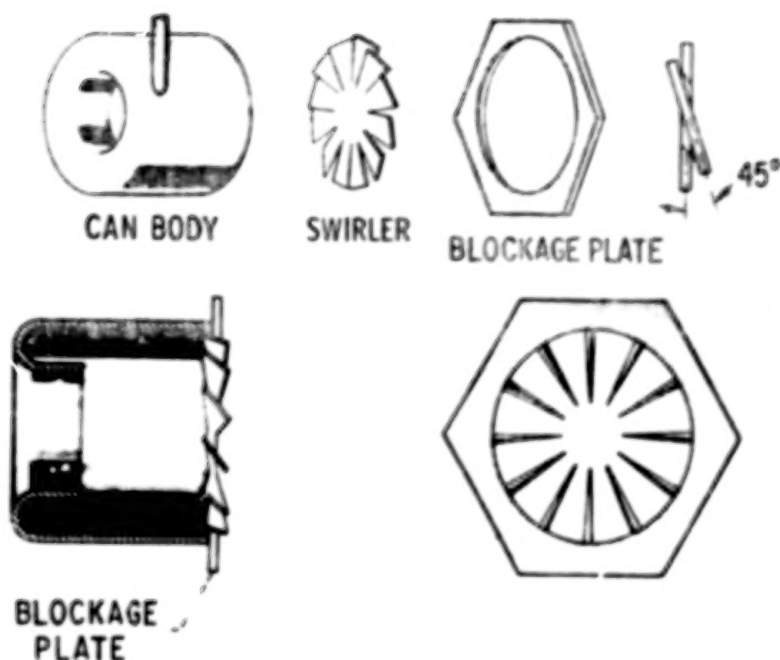


Figure 9. Details of NASA Swirl-Can Module

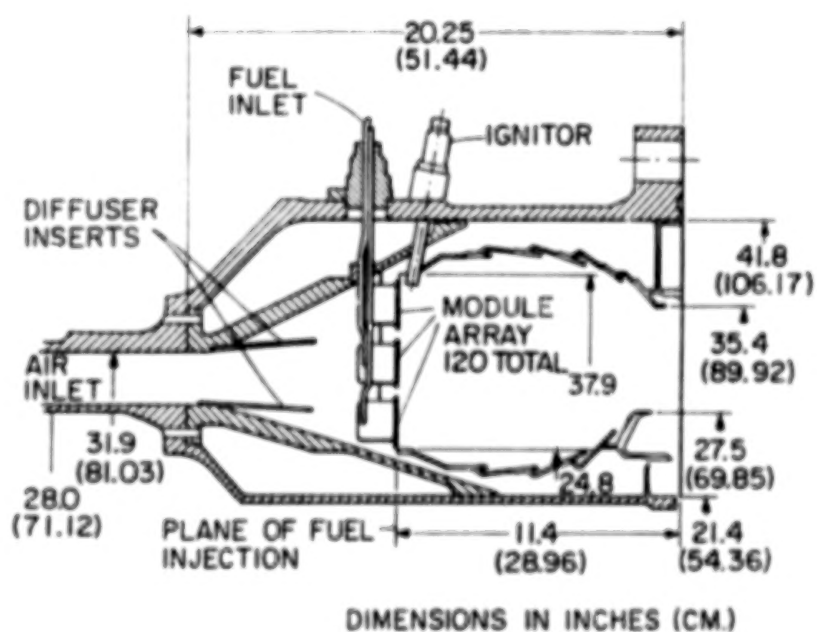


Figure 10. Tangential View of NASA Swirl-Can Combustor Annulus

with the air which passes between the modules but is not entrained into the immediate wakes will make the combustion products even leaner, rapidly decreasing the rate of nitric oxide formation. This effect can be seen in Figures 3 through 6. Regardless of which curve is applicable to the case of interest, at sufficiently low equivalence ratios the nitric oxide formation rates fall off sharply as the equivalence ratio decreases. Therefore, the complete nitric oxide formation process can be modeled in this limit as the products of a stirred-reactor module-wake primary zone being suddenly quenched and then simply diluted to the overall fuel-air ratio. This model corresponds to the separate module wake combustion which is observed at low fuel-air ratios.

An uncertainty encountered in analyzing the NASA combustor is that contrary to more conventional designs, the volume of the primary zone and the mass flow of air entering this zone are not well defined by the liner geometry. The fluid mechanics of entrainment into a reacting, swirling, recirculating flow are not tractable enough to be used in the relatively simple nitric oxide formation model being proposed here. The following assumptions are made to obtain simple models: (1) The volume of the primary zone in the wake of each swirl can module is taken to be  $8.7 \text{ in}^3$ , which is equal to the area of an averaged blockage plate multiplied by the plate's diameter. This aspect ratio of approximately one is verified by cold-flow tests. If the flow patterns in the combustor do not change much as the volume flow rate and combustion intensity are varied, the volume of the



primary zones will remain nearly constant. Of course, as the fuel-air ratio approaches stoichiometric and the primary zones coalesce, this assumption becomes invalid. (ii) The average fuel fraction in the primary zones is proportional to the combustor's overall fuel fraction. Once again, if the combustor's flow patterns remain relatively fixed, this assumption will be approximately true.

A few comments on the above modeling assumptions are in order. (i) Primary zone residence times are proportional to primary zone volume. Nitric oxide production is found to be almost linear with residence time for the region of interest, so that changing the primary zone volume will approximate sliding the nitric oxide prediction curves vertically on a log scale. (ii) Changing the proportionality factor between the primary and overall fuel fractions is equivalent to changing the fraction of the overall air flow which enters the primary zone. This changes both the primary zone residence time and the dilution factor on exit from the primary zone. The approximate linearity of nitric oxide with residence time mentioned above results in a cancellation of the residence time and dilution factor effects. Thus, changing the proportionality factor between the primary and overall fuel fractions merely slides the nitric oxide predictions horizontally on a log scale of overall fuel-air ratio.

In the limit of overall fuel-air ratios near stoichiometric, so much fuel is being added to the flow through the swirl cans that combustion conditions in the module wakes are much richer than

stoichiometric. As mixing occurs with the air which passes between the modules but is not entrained into the immediate wakes, the rate of nitric oxide formation will increase markedly. This effect is shown in Figures 3 through 6. Regardless of which curve is applicable to the case of interest, at equivalence ratios greater than unity, the nitric oxide formation rates are significantly lower than the rates prevailing after dilution to an equivalence ratio near unity. It is also found that residence times calculated for the module wakes are several times shorter than the overall residence times calculated for the combustor. For the above reasons, the nitric oxide formed in the module wakes can be neglected compared to that formed after dilution to the overall fuel-air ratio. Therefore, the complete nitric oxide formation process can be modeled in this limit as the whole combustor volume operating as a stirred reactor at the overall fuel-air ratio. This model corresponds to the "ring of fire" type of combustion observed at fuel-air ratios near stoichiometric.

Since the entire combustor liner annulus is serving as the combustion zone of interest, the volume of the zone as well as the mass flow rates through it are well defined by the liner geometry. The volume of the annulus is approximately  $4.1 \text{ ft}^3$ . The average fuel fraction is about 1.03 times the overall to allow for one half of the liner cooling air to participate in the reactor on the average.

Predictions from the two limiting case models have been published previously by Heywood and Mikus (3). They serve as an important backdrop for the more complete model which is implemented

later in this subsection. Predictions are expressed as nitric oxide mass fraction  $\{NO\}$ . These may be converted to the emission index  $E_{NO_2}$  by the formula

$$E_{NO_2} = 1.53 \frac{\{NO\}(1+f)}{f} \times 10^3 \sim 1.53 \frac{\{NO\}}{f} \times 10^3 \quad (24)$$

where  $f$  is the overall fuel-air ratio. Calculations have been done for both the residence time distribution of equation (17) and for a uniform residence time; these predictions differ by only a few percent. The latter method has been used for the predictions presented in this subsection.

Figures 11 through 13, and 14, show these limiting-case predictions as dashed lines, for two different inlet air temperatures. Data points shown in these figures were derived from NASA data (4). The data points shown as circles are measurements made at a combustor inlet pressure of 5 to 6 atm, with a combustor air flow of 85 to 110 lbm/sec. The data points shown as diamonds are known to be measured at 6 atm and 110 lbm/sec, which were the values used in the prediction computations. The solid curves in these figures include the dilution zone model, and will be described later in this subsection.

The dashed curves drawn for fuel-air ratios between 0.01 and 0.03 are calculated with the low fuel-air ratio model, using a primary zone fuel fraction 2.5 times the overall value. As mentioned earlier, a change in this parameter will simply proportion out the prediction

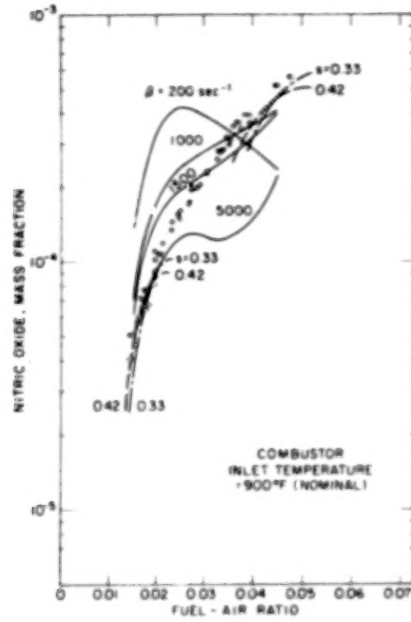


Figure 11. Comparison of  $\text{NO}_x$  Predictions with NASA Swirl-Can Data (4) for Various Values of a Constant Mixing Intensity (solid curves); fixed primary zone parameters.

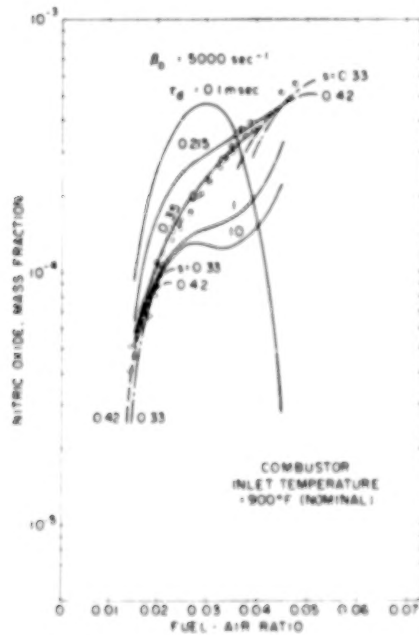


Figure 12. Comparison of  $\text{NO}_x$  Predictions with NASA Swirl-Can Data (4) for Various Values of Mixing Intensity Decay Time (solid curves); fixed primary zone and initial intensity.

curves horizontally. Also note that a change in primary zone volume simply shifts the curves vertically. The mixing parameter values 0.33 and 0.42 which are illustrated produce approximately the proper slope to match the data, especially for the higher combustor inlet temperature case, Figures 11 through 13.

The dashed curves drawn for fuel-air ratios greater than 0.03 are calculated using the model appropriate to fuel-air ratios comparable with stoichiometric. Here the primary zone volume and fuel-air ratios are well defined, so that the prediction curves are not shiftable without making basic changes in the model.

Having matched the emissions data with the limiting-case models, the following model parameters can be assigned approximate values for this combustor: (i) primary zone volume  $V_p \approx 8.7 \text{ in.}^3$  (ii) primary to overall fuel fraction factor  $F_p/F_o \approx 2.5$  and (iii) primary zone mixing parameter  $s_p \approx 0.4$ . It should be noted that these parameters were only evaluated approximately, and that they by no means represent the best possible match with the experimental data. However, these parameter values are adequate for exploring the potential of the dilution zone model to predict nitric oxide formation over a wider range of combustor fuel-air ratios.

The dilution zone calculation is in fact an extension of the lean end primary zone calculations. As described at the end of Subsection 2.3, the dilution zone is linked in by adding additional fluid elements for the dilution air. In this case these new elements represent the air flow which has passed between the modules, but

was not entrained into the recirculating wake primary zone. For a primary zone enrichment factor  $F_p/F_o = 2.5$ , only about 40% of the air flow passes through the primary zone. So for a dilution zone ensemble of 750 elements, about 300 are carried over from the primary zone ensemble, and 450 will start out as additional air elements. Starting from this condition, the mixing and  $NO_x$  calculations are carried forward as described in Subsection 2.3.

Figure 11 presents the mixing model predictions for a range of values of the mixing parameter  $\beta$ , assuming that in each case  $\beta$  is constant in time. At a given fuel-air ratio, the behavior of the nitric oxide predictions as a function of  $\beta$  can be understood by examining the history of the nitric oxide formation rate as the flow from the primary zone is mixed with the dilution air. For example: (1) At overall fuel-air ratios less than about 0.02, the primary zone is leaner than the value for peak nitric oxide formation. As the flow from the primary zone is diluted, the nitric oxide formation rate decreases sharply, becoming negligible long before the overall fuel-air ratio is reached. Therefore, a high value of  $\beta$  representing rapid dilution of the flow leaving the primary zone would predict nitric oxide levels just slightly higher than the rapid-quench model represented by the dashed lines. On the other hand, the gradual dilution of primary zone products represented by a low value of  $\beta$  allows nitric oxide to continue being formed at a significant rate for a longer time, yielding a higher predicted

value. (ii) At overall fuel-air ratios in the vicinity of 0.045 the primary zone is considerably richer than the value for peak nitric oxide formation. As dilution of the primary zone flow occurs, the nitric oxide formation rate at first increases strongly and then decreases sharply once diluted below the fuel-air ratio of peak nitric oxide formation. In this region, a high  $\beta$  value represents rapid dilution past the nitric oxide formation peak, while a low  $\beta$  value represents a slow dilution toward the peak. Intermediate values of  $\beta$  allow the dilution process to dwell near the nitric oxide formation peak for significant periods of time, yielding high nitric oxide predictions.

A better description of the time history of the mixing intensity  $\beta$  is to realize that it is a function of the intensity of turbulent fluctuations within the combustor. Turbulence is generated at the entry plane by the flow passing through the blockage plates and swirlers and by the combustion in the primary zone. But once the flow leaves the primary zone and dilution begins, the turbulence decays. One possible assumption for the form of the corresponding decay of  $\beta$  is

$$\beta = \beta_0 \exp (-t/\tau_d) \quad (25)$$

where  $\beta_0$  is the initial  $\beta$ ,  $t$  is the time elapsed since exit from the primary zone, and  $\tau_d$  is a characteristic decay time. A  $\beta_0$  of about  $5000 \text{ sec}^{-1}$  approximates the initial mixing intensity as can be seen

from the low fuel-air ratio regime of Figure 11 where the initial rate of quenching is the most important factor. The value of  $\beta_0$  will be examined later. Figure 12 shows predicted nitric oxide levels for a range of values of  $\tau_d$ , the characteristic decay time. For comparison, the total combustor residence time is 5-6 msec. Note that for a decay time longer than this residence time, the predictions are nearly the same as for a constant  $\beta$  of 5000 as shown in Figure 11. A short decay time is qualitatively like the smallest value of constant  $\beta$  case shown in Figure 11. Intermediate values of decay time yield results which match the data closely; a decay time of 0.35 msec will be used for further calculations. This value of  $\tau_d$  suggests that the turbulent energy, generated by the swirlers and blockage plates at the combustor entrance plane, is dissipated within a distance of order one blockage plate diameter.

From equation (22) it can be derived that for a given combustor residence time, the total number of mixing interactions is proportional to the time integral of the mixing intensity  $\beta$ . If equation (25) holds, the time integral of  $\beta$  is approximately  $\tau_d \beta_0$ , assuming that the residence time is much longer than the decay time  $\tau_d$ . For the case of rapidly decaying  $\beta$  the nitric oxide predictions should not be too sensitive to changes in  $\beta_0$  and  $\tau_d$  provided the product  $\tau_d \beta_0$  is fixed. This effect is illustrated in Figure 13 for a  $\tau_d \beta_0$  product of 1.75. The differences are most marked at overall fuel-air ratios around 0.02, where the initial dilution rate is most important.

Choosing the mixing intensity history



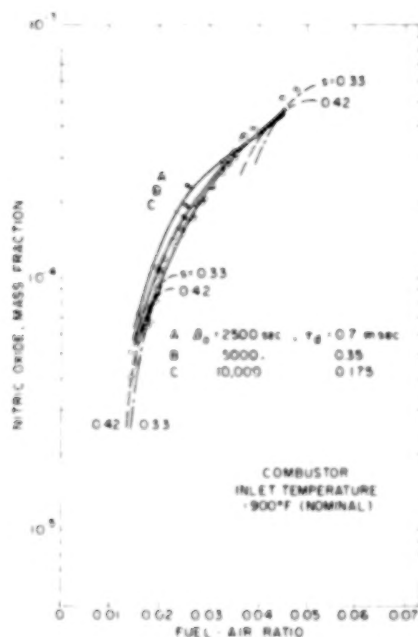


Figure 13. Comparison of  $\text{NO}_x$  Predictions with NASA Swirl-Can Data (4) for Various Initial Mixing Intensity/Decay Time Pairs (solid curves); fixed primary zone and pair product.

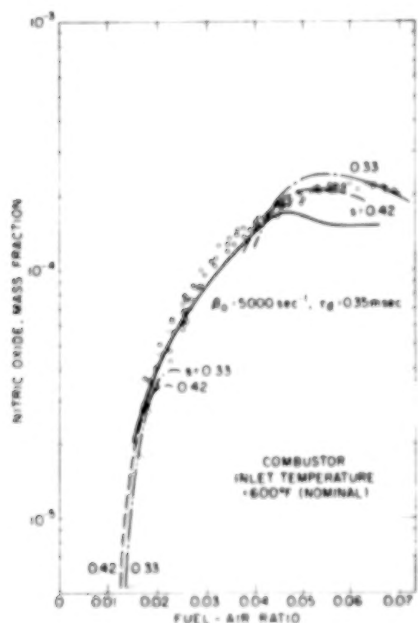


Figure 14. Comparison of  $\text{NO}_x$  Predictions with NASA Swirl-Can Data (4) using Parameter Values Fit at Different Inlet Temperatures (solid curve)

$$\beta = 5000 \exp(-t/0.35 \text{ msec}) \text{ sec}^{-1} \quad (26)$$

as a reasonable match to emission data at 900 °F inlet temperature, the predictions were recalculated for an inlet temperature of 600 °F. The results are presented in Figure 14. The predicted nitric oxide levels are close to the actual data, falling somewhat lower near the overall stoichiometric fuel-air ratio of 0.069. However, some of the model parameters, such as the primary zone mixing parameter  $s_p$ , and functional form of  $\beta(t)$ , were evaluated only approximately. The curve shown in Figure 14 is not necessarily the best match to the experimental data.

Possible mixing model refinements which were evaluated were as follows: (i) Calculate the primary zone nitric oxide formation by using equation (17) rather than assuming uniform residence times for all the fluid elements in the distributions. (ii) Allow the mixing intensity to decay toward some non-zero value characteristic of "pipe-flow turbulence" rather than decaying toward zero. Neither of these modeling refinements produced significantly better predictions.

A third refinement which was not evaluated would be to attempt to reach a given level of mixing parameter  $s$  at the combustor exit. This value is about 0.5 for the calculations in Figures 13 and 14 which is higher than the values of 0.33-0.42 found to give a better match to the data in the stirred reactor model for high fuel-air ratios

described earlier in this subsection.

Table 5 presents some data relevant to the  $\text{NO}_x$  model calculations presented in Figure 12 (the " $\tau_d = 0.35$  msec" curve) and also in Figure 13 as curve B.

TABLE 5  
Data Relevant to a  $\text{NO}_x$  Prediction Curve  
for the NASA Swirl-Can Combustor

Overall Fuel-Air Ratio	Primary Zone Fuel-Air Ratio	Primary Zone Residence Time msec	Total Residence Time msec	Number of Mixing Interactions	Nitric Oxide Mass fraction
0.015	0.0375	0.88	3.99	441	$5.69 \times 10^{-5}$
0.025	0.0625	0.73	3.24	440	$1.76 \times 10^{-4}$
0.035	0.0875	0.71	2.88	439	$3.09 \times 10^{-4}$
0.045	0.1125	0.73	2.70	438	$4.53 \times 10^{-4}$

inlet temperature = 760 K (907 °F), pressure = 5.8 atm (85.6 psia),  
mixing intensity as in equation (26).

#### 4. Operating Characteristics of the NASA Combustor Inferred from $\text{NO}_x$ Data

The matching of model predictions to measured  $\text{NO}_x$  emissions data has identified several operating characteristics of the NASA swirl can combustor. These can be compared with the requirements outlined in Subsection 2.2 for substantially reducing  $\text{NO}_x$  emission levels below current technology values, viz. a fuel lean primary zone, short primary zone residence time, significantly more uniform fuel-air mixing within the primary zone, and rapid dilution of the primary zone burst gases.

This analysis indicates that the average fuel-air ratio in the module wake, the primary combustion zone, is fuel lean for overall fuel-air ratios lower than about 0.026. A ratio of about 2.5 between primary zone and overall fuel fraction gives a good fit to the data. Thus at take-off conditions for current large engines (an overall fuel-air ratio of about 0.023) the primary zone equivalence ratio is about 0.87 which is close to the peak NO formation rate in Figures 4 and 5 for nonuniform mixtures. Greater entrainment of air into the primary zone than occurs in the current combustor design would therefore be desirable.

The values of  $s$  found necessary to match the data (about 0.4) are also not significantly better than is achieved with current technology combustors. A previous review <sup>(3)</sup> indicated that  $s$  values between 0.3 and 0.7 matched  $\text{NO}_x$  emissions data obtained from conventional combustors. If the primary zone in the NASA swirl can be leaned out further, as suggested in the previous paragraph, then Figures 3 through 6 indicate

that significantly better mixing in the module wake would improve the  $\text{NO}_x$  emission characteristics.

The primary zone residence time is 0.7 - 0.9 msec, which is below conventional combustor values. Thus, some reduction in  $\text{NO}_x$  emissions has been achieved through the use of many modules each with its own primary zone.

A comparison of the dashed lines in Figures 13 and 14 with the dilution zone model predictions (solid lines) indicates that at overall fuel-air ratios of about 0.025 a significant part of the exhaust NO has been formed in the dilution zone, downstream of the primary zone exit. The mixing model studies suggest that within about one blockage plate diameter of the primary zone exit this dilution occurs rapidly. However, the mixing intensity then decays. Increasing the mixing intensity between dilution air and primary zone exit gases would further reduce  $\text{NO}_x$  emissions.

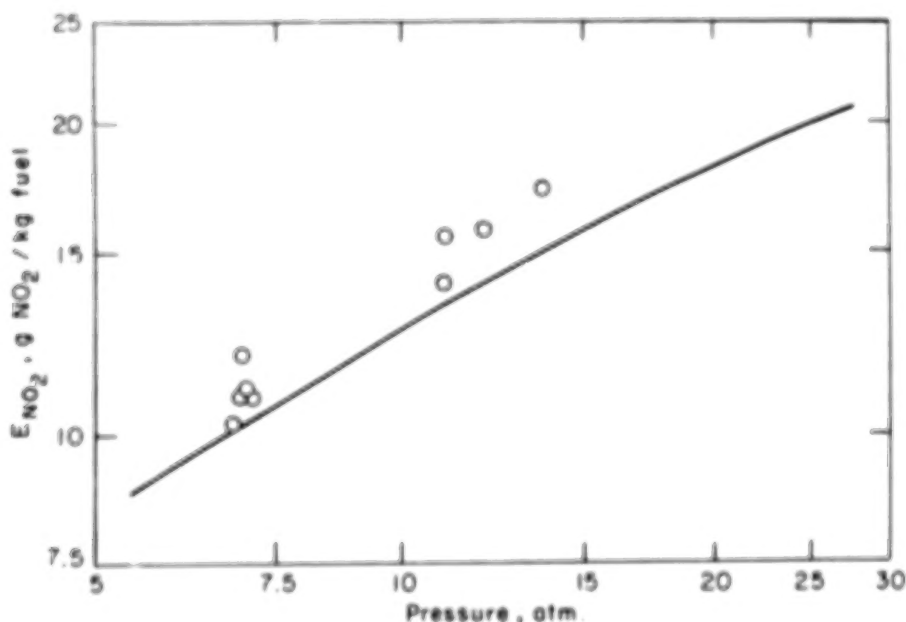


Figure 15.  $\text{NO}_x$  Predictions versus Pressure for a NASA Swirl-Can Module, Baseline Case; see text for details; circles are test rig data obtained by NASA (16)

## 5. Parametric Studies

Two parametric studies are presented in this section. The goal of the first study is the extrapolation of  $\text{NO}_x$  emission index data obtained from a combustor test rig. In particular, it was desired to extrapolate from test rig pressures to the higher pressures typical of engine operating conditions. For this study the externally imposed factors were as follows: air inlet temperature = 733 K (860 °F), overall fuel-air ratio = 0.02 (for kerosene fuel), reference velocity = 30 m/s (100 ft/s), pressure ranging from 6 to 25 atm.

Modelling parameters determined in Subsection 3.2 were used as baseline values ( $s_p = 0.4$ ,  $F_p/F_o = 2.5$ ,  $V_p = 8.7 \text{ in}^3$ ,  $\beta_o = 5000 \text{ sec}^{-1}$ , and  $\tau_d = 0.35 \text{ msec}$ ). Figure 15 shows the baseline predictions plotted against pressure, assuming that the modelling parameters are not functions of pressure. The circles in this figure are test rig measurements obtained by NASA. The predictions are in close agreement with the data in both absolute level and pressure trend over the range of available data. This gives some credibility to the predictions at the high pressures. The  $\text{NO}_x$  predictions do not lie along a straight line in this log-log plot against pressure. The curve is almost linear at low pressures, but the slope decreases at higher pressures due to the increasing importance of NO-consuming reactions as equilibrium is approached. For the conditions pertaining to this baseline condition, the pressure dependency of the emission index can be expressed as  $p^{0.59}$  between 6 and 10 atm, decreasing to  $p^{0.48}$  between 15 and 25 atm. These are comparable to the simple  $p^{1/2}$  dependency often quoted in the literature, e.g.,

Heywood and Mikus (3). The  $p^{1/2}$  dependency is based upon a constant burned gas temperature, rather than the constant inlet air temperature used in this section.

NASA has experimented with many different swirl-can geometries (16);  $\text{NO}_x$  emissions pressure dependency has ranged from  $p^{0.13}$  to  $p^{0.79}$ . One objective of this parametric study was to see if modest variations of the parameter values would significantly change the pressure dependency of the  $\text{NO}_x$  predictions.

In order to test the sensitivity of the  $\text{NO}_x$  predictions to variations in the modelling parameters for this type of extrapolation, each of the five parameters was varied one at a time. The resulting predictions are shown in Figure 16. Curves have been drawn for the case of modelling parameters which do not change with pressure. The effect of parameters which do change with pressure will be discussed later.

Figure 16a shows that the predictions are rather insensitive to small variation in the primary zone mixing parameter  $s_p$  for this particular baseline. This is due to the mean equivalence ratio (0.75) of the primary zone which results from values of the overall fuel-air ratio (0.02) and the primary zone enrichment parameter (2.5). As can be seen in Figures 3-6, in the vicinity of  $\bar{\phi} = 0.75$ , the  $\text{NO}_x$  formation rate is reasonably insensitive to  $s_p$ . Note that there would be a great sensitivity at  $\bar{\phi}_p = 0.5$ , for example, which would be the case for combustor operation at an overall fuel-air ratio of 0.013.

Figure 16b shows the sensitivity of modelling prediction to variation in primary zone enrichment factor. For the case being calculated, the values  $F_p/F_o = 2.75, 2.5$ , and  $2.25$  correspond to primary zone equivalence ratios  $\bar{\phi}_p = 0.83, 0.75$ , and  $0.67$ , respectively. Referring

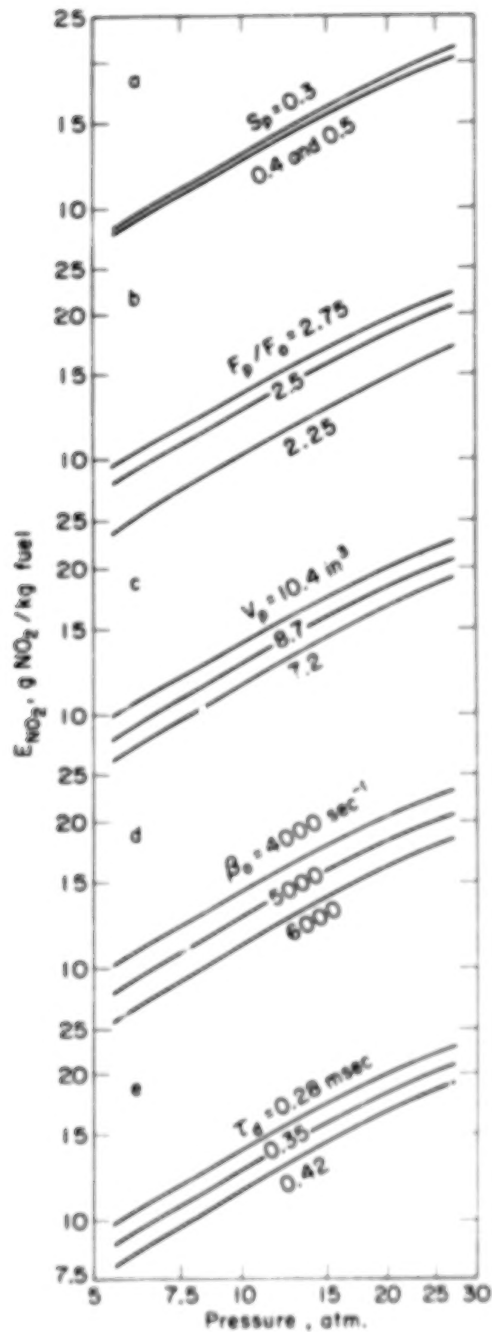


Figure 16.  $\text{NO}_x$  Predictions versus Pressure for a NASA Swirl-Can Module, Parametric Study; see text for details middle curve of each trio is baseline case (Figure 15)



again to Figures 3 through 6, for  $s_p = 0.4$  the primary zone  $\text{NO}_x$  formation rate is a very weak function of  $\bar{\phi}_p$ . However, in the dilution zone the leaner mixtures will be more readily "quenched" to negligibly small  $\text{NO}_x$  formation rates. This explains the sensitivity to primary zone enrichment factor apparent in Figure 16b.

Sensitivity of the  $\text{NO}_x$  predictions to primary zone volume is presented in Figure 16c. As noted in Subsection 3.2,  $V_p$  is proportional to the primary zone residence time, and primary zone  $\text{NO}_x$  is nearly linear with this time. However, for the case under consideration, significant  $\text{NO}_x$  is formed in the dilution zone; independent of  $V_p$ . Thus, the overall dependency of  $\text{NO}_x$  on  $V_p$  is less than linear. This dependency is slightly weaker at high pressures, since NO comes closer to equilibrium levels.

Figures 16d and e demonstrate the effects of varying dilution zone parameters. For a fixed mixing decay time  $\tau_d = 0.35$  msec, higher values of the initial mixing intensity represent earlier, more complete mixing. Since the current case has a lean primary zone, this mixing simply leans out the primary zone products, thus quenching  $\text{NO}_x$  formation. This influence of  $\beta_0$  is shown quantitatively in Figure 16d. The parameter  $\tau_d$  has a similar but less marked effect. For a fixed  $\beta_0 = 5000 \text{ sec}^{-1}$ , higher values of  $\tau_d$  represent more complete mixing. However, for a given degree of mixing, the mixing does not occur as early as it did for higher values of  $\beta_0$ . Figure 16e presents the  $\text{NO}_x$  predictions for a range of  $\tau_d$ .

None of the curves in Figure 16 exhibit a  $\text{NO}_x$  prediction pressure dependency which is noticeably different from the baseline case. There-

fore, experimentally observed pressure dependencies which differ significantly from the trend of the baseline case must be explained in terms of pressure-dependent modelling parameters.

The effects of modelling parameters which vary with pressure can be assessed as in the following example. In Figure 16c, imagine a line drawn from low pressure end of the  $V_p = 10.4 \text{ in}^3$  curve, to the high pressure end of the  $V_p = 7.2 \text{ in}^3$  curve. This would correspond to a primary zone whose volume decreases by 31 percent as the operating pressure increases by a factor of 5. The slope of that imaginary line would be 0.41, implying a pressure dependency of  $p^{0.41}$  for the  $\text{NO}_x$  emissions. In this way, a range of pressure dependency exponents can be explained in terms of modelling parameters which vary with pressure. Current understanding of the five modelling parameters is insufficient to allow calculation of how they might change with combustor operating conditions.

The second parametric study examined operation of the NASA swirl-can combustor at conditions typical of state-of-the-art jet engines. The modelling parameters were investigated with the goal of improving the predicted  $\text{NO}_x$  emission index. In this case the externally imposed factors were: air inlet temperature = 775 K (935 °F), pressure = 23 atm, overall fuel-air ratio = 0.023 (kerosene fuel again), and reference velocity = 18 m/s (60 ft/s).

Once again, modelling parameter values from Subsection 3.2 were used as a baseline. The baseline emission index prediction is 38 g  $\text{NO}_2$ /kg fuel. This is comparable to measured values for conventional combustors. The emission index should be decreased to approximately 10 g/kg fuel in order to meet proposed emission standards. It

was not possible to predict an emission index less than 10 by reasonable variations of a single modeling parameter from the baseline case. The modeling parameters were therefore varied in pairs in order to explore and take advantage of their interactions. Results are presented in Figures 17 through 20. For reference, the baseline primary zone equivalence ratio  $\bar{\phi}_p = 0.87$ .

Figure 17 presents emission index predictions for ranges of  $s_p$  and  $s_o$ . As can be seen in Figure 5, the primary zone  $\text{NO}_x$  should decrease with increasing  $s_p$ ; and due to the lean primary zone, more intense mixing will simply quench the  $\text{NO}_x$  reactions faster. Similar results for ranges of  $s_p$  and  $\tau_d$  are shown in Figure 18. However, neither of these pairs of varied parameters predicted an emission index significantly below 20. At this mean primary zone equivalence ratio, simply changing mixing rates is not the answer to significantly lower  $\text{NO}_x$  emissions.

The effects of  $V_p$  and  $F_p/F_o$  for the current case are presented in Figure 19. Primary zone enrichment factors  $F_p/F_o = 1.5, 2.0, 2.5$ , and 3.0 correspond to  $\bar{\phi}_p = 0.51, 0.69, 0.87$ , and 1.05, respectively. Again referring to Figure 5, for  $s_p = 0.4$  the primary zone  $\text{NO}_x$  formation rates are roughly equal for  $\bar{\phi}_p = 0.87$  and 0.69, somewhat lower for  $\bar{\phi}_p = 1.05$ , and approximately a factor of 2 lower for  $\bar{\phi}_p = 0.51$ . This relative ranking is observed in Figure 19 at the high end of the  $V_p$  scale, where long primary zone residence times overshadow dilution zone processes. For low values of  $V_p$  the dilution zone has a higher relative significance. The rich primary zone corresponding to  $F_p/F_o = 3.0$  continues to form  $\text{NO}_x$  well into the dilution process, thus overtaking the leaner primary zone predictions. Varying only  $V_p$  and  $F_p/F_o$ , emission

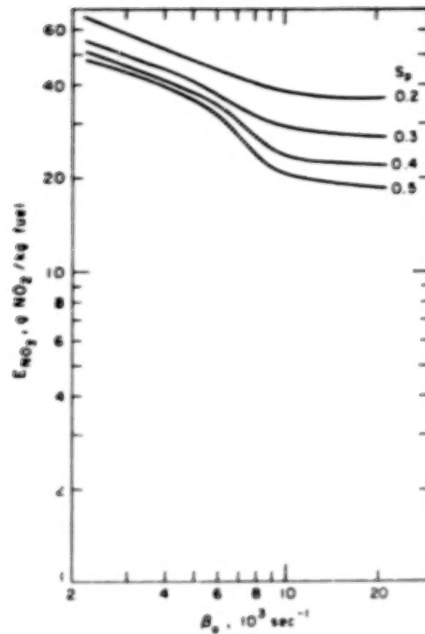


Figure 17.  $\text{NO}_x$  Predictions versus Initial Mixing Intensity for Various Values of Primary Zone Nonuniformity, Typical Engine Conditions; see text for details

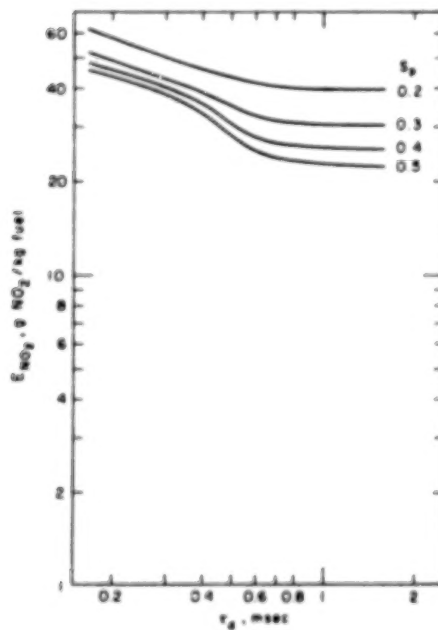


Figure 18.  $\text{NO}_x$  Predictions versus Mixing Intensity Decay Time for Various Values of Primary Zone Nonuniformity, Typical Engine Conditions; see text for details

indices lower than 10 are achieved only for very lean, small primary zones. Unfortunately, this combination is likely to produce an unacceptable level of CO due to incomplete combustion (not included in this modeling effort). Thus, variations which do not consider mixing are also not the answer to low  $\text{NO}_x$  in this case.

More promising predictions are presented in Figure 20, where  $s_p$  and  $F_p/F_o$  are varied. These results are fundamentally similar to Figure 5, but include the effects of finite residence time and a dilution process. An emission index lower than 10 is predicted in this case for a lean, well-mixed primary zone, e.g.  $F_p/F_o \lesssim 1.75$  ( $\phi_p \lesssim 0.60$ ) for  $s=0.2$ .

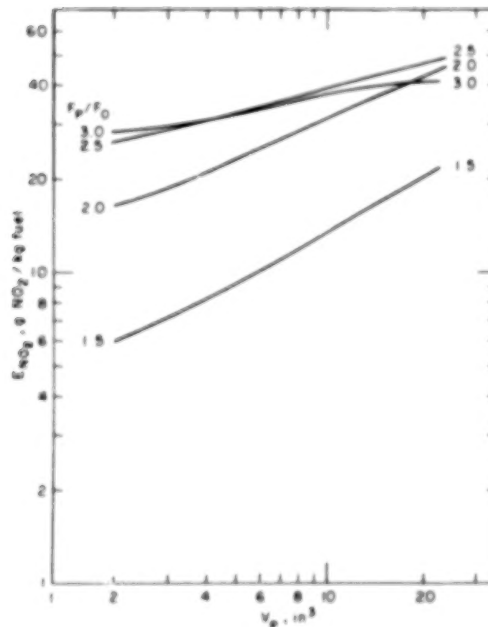


Figure 19.  $\text{NO}_x$  Predictions versus Primary Zone Volume for Various Values of Primary Zone Enrichment Factor, Typical Engine Conditions; see text for details

## 6. Air Flow Streamline Calculations

As a first cut in understanding the flow field downstream of the NASA swirl-can modules, an existing finite-difference computer program was adapted. This program was TEACH-T developed by Spalding et al, (17), which calculates steady, non-swirling, recirculating, axisymmetric, turbulent flow fields. The boundary conditions were set up as diagrammed in Figure 21: a cylinder with cross-sectional area equal to the liner area per module at the blockage plate plane of the full NASA combustor; zero velocity at the walls; at the blockage plate plane no flow at swirler hub radii, uniform axial flow at swirler vane radii, no flow at blockage plate radii and uniform axial flow at radii between the blockage plate and the cylinder wall; zero pressure gradient 4.5 diameters downstream of the blockage plate; and 19 percent of the mass flow passing through the swirler (see Subsection 9.2). Within the flow field gas properties were taken to be those of ambient air.

Figure 22 is a streamline plot derived from the computer calculation for 38 m/s (124 ft/s) mean axial velocity. The flow is from left to right. The streamlines toward the top of this figure represent the annular jet issuing from the gap between the blockage plate and the cylinder wall. Four streamlines can be seen emerging from the swirler; they move rapidly outward, so that the angular velocity of this flow in the real system would be lost quite early. The swirler streamline closest to the axis of symmetry (bottom of the figure) is the contour of zero stream function, and thus outlines the mean recirculation zone. This zone extends about 1.8 blockage plate diameters down-

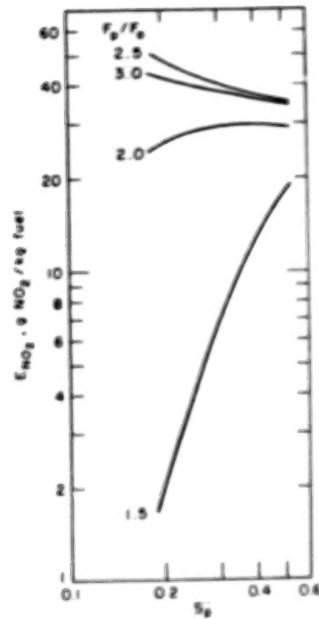


Figure 20.  $\text{NO}_x$  Predictions versus Primary Zone Nonuniformity for Various Values of Primary Zone Enrichment Factor, Typical Engine Conditions; see text for details.

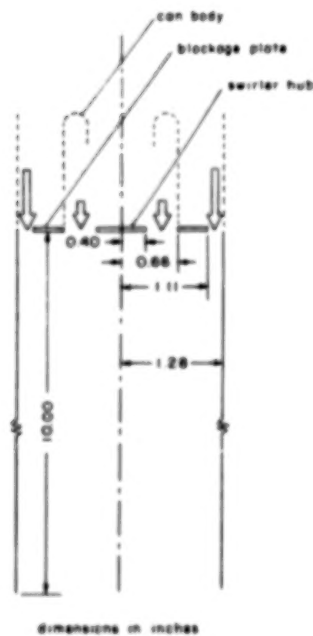


Figure 21. Schematic of Boundary Conditions for Numerical Flow Calculations.

stream and about 13% of the total flow is involved in recirculation. It must be noted that these are the mean streamlines calculated for this turbulent flow field; they do not show the turbulent mass transfer which crosses such streamlines.

Streamline calculations were also performed for 9 m/s (31 ft/s) axial velocity, with virtually no change in the streamline pattern. This represents a range of Reynolds numbers of 35,000 to 140,000, based on blockage plate diameter. From these calculations it follows that the size of the module wake primary zone, and the fraction of the air which passes through it are weak functions of combustor operating conditions. This supports the choice of  $V_p$  and  $F_p/F_o$  as primary zone parameters which are fixed for a given combustor geometry. In addition, the value chosen for  $V_p$  ( $8.7 \text{ in}^3$ ) is of the right order.

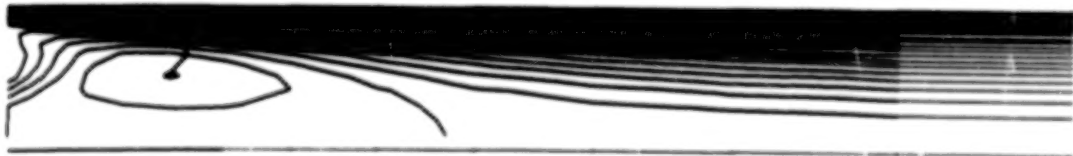


Figure 22. Streamline Plot of Calculated Flow Field; flow is from top to bottom, with symmetry axis at left side



## 7. Calculation of Fuel Droplet Evaporation

As argued in Subsection 2.2, the air flow pattern and early fuel processes are of fundamental importance for determining  $\text{NO}_x$  formation. Section 6 dealt with the calculation of air flow; this section will address the fuel processes.

As will be seen in Subsection 8.2, fuel droplets are formed by the breakup of sheets and ligaments associated with the swirler vanes. The maximum stable droplet size may be calculated as suggested by Prandtl (18, p. 326)

$$d \approx 15.4 \frac{\sigma}{\rho v^2} \quad (27)$$

where  $\sigma$  is the fuel's surface tension,  $\rho$  is the air density, and  $v$  is the relative velocity between fuel and air. This equation will be verified in Subsection 8.2. For a given fuel  $\sigma$  is a function of temperature, so it is necessary to know the temperature of the fuel droplet; this was assumed to be the wet bulb temperature, or 0.99 times the absolute boiling temperature, whichever was lower. The quantity  $\rho v^2$  was calculated for inlet conditions using the open area at the plane of the blockage plate.

A computer program was written to calculate the evaporative flight of a fuel droplet. Komiyama (19, Appendix 3) described a similar program. Stagnant droplet evaporation rates based upon Goldsmith and Penner (20) were corrected for forced convection

following Ranz and Marshall (21). Droplet acceleration from an initial state of rest was calculated using the standard drag equation for a sphere, corrected for evaporation effects according to Spalding (22). Calculations were conducted for projected idle and maximum cruise power conditions; evaporation would be somewhat faster at take-off. Conditions for the gas surrounding the fuel droplets were taken to be alternately inlet conditions and combustor exhaust conditions. Even the latter assumption is rather conservative since it is far below the combustion temperatures expected in the flame zone. Table 6(a) presents the results of these calculations. The higher gas temperature assumptions predict essentially complete evaporation in less than 0.1 module diameter, even at idle. This supports the assumption of instantaneous evaporation which was made in the  $\text{NO}_x$  model. Note, however, that at idle a fuel droplet would evaporate relatively slowly in regions not heated by combustion products.

Similar calculations were done for an ambient pressure and temperature simulation which will be described in subsection 10.2. These results are shown in Table 6(b). It was hoped that pentane, which has a normal boiling point of 309 K, would be sufficiently volatile to simulate the evaporation of kerosene at the higher temperatures to which it would be exposed in an engine's combustor. However, due to lower gas density and somewhat higher surface tension, the pentane droplets are significantly larger [see equation (27)]. For a nominal gas temperature of 1000 K, the pentane requires more than

one module diameter to evaporate, even at simulated cruise conditions. This explains the experimental difficulties which will be discussed in subsection 10.2.

TABLE 6

Fuel Droplet Evaporation Parameters and Calculated Results for Engine Conditions and a Simulation

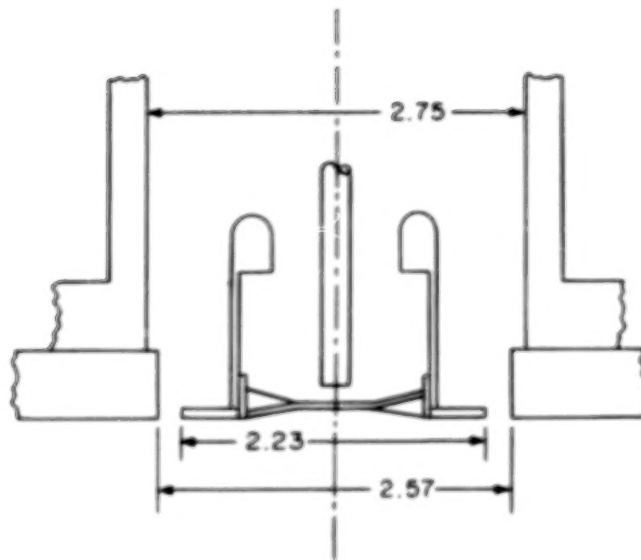
	(a) kerosene fuel estimated				(b) pentane fuel simulated	
	<u>idle</u>		<u>cruise</u>		<u>idle</u>	<u>cruise</u>
pressure, atm	4.2		13.2		1	1
gas temperature, K	482	1005	763	1533	1000	1000
fuel temperature, K	441	524	580	617	306	306
gas velocity, m/sec	49	49	62	62	49	64
initial drop size, $\mu$	21	13	22	11	75	43
99% evap. time, msec	5.95	0.16	0.56	0.04	5.3	1.9
distance, module d's	4.99	0.07	0.52	0.01	2.3	1.1

## 8. Flow Visualization Experiments

### 8.1 Flow hardware

A program of flow visualization experiments was undertaken in order to obtain a better qualitative understanding of the flow field in the NASA swirl-can combustor. A stainless steel blockage plate was made with area equal to the average area of the 120 blockage plates in the full NASA combustor. This plate was silver soldered to a standard swirler. A plexiglass can body was fashioned and pressed onto the swirler. This assembly was mounted by two struts, centered in and flush with the downstream face of a thick plexiglass flange whose open area was equal to the liner area per module in the full NASA combustor. The flange was bolted to the downstream end of a slightly larger plexiglass tube. A fuel tube was fashioned such that it terminated 1/8 inch upstream of the swirler with a 3/16 inch tube having an 0.052 inch orifice at the end; this tube could be aimed at any part of the swirler during the experiments. Details of the visualization test section are shown in Figure 23.

Air was supplied to this test section from a 200 cfm compressor through a pressure regulator, throttling valve, ASME orifice rig, flow straightener, and 20 diameters of straight pipe. The test section generally discharged directly into the room, and ambient condition prevailed at the module. The air flow rate was controlled so that reference velocities could match those of the full NASA combustor. Reynolds numbers based on blockage plate diameter were of order  $10^5$ .



dimensions in inches

Figure 23. Diagram of Visualization Test Section  
flow is from top to bottom



Figure 24. Helium-filled Soap Bubble Traces in  
Module Wake; mean flow is from top  
to bottom; bubbles are injected at  
tip of recirculation zone

## 8.2 Techniques and Results

The size of the recirculating wake downstream of the module was determined by probing with a wool tuft. Probing along the axis of the flow field, a length of 1.0 module diameter was observed; this increased to 1.8 diameters when a confining tube section was added downstream of the module; no Reynolds number effect was observed. These results quantitatively confirm results of the flow calculations presented in Section 6; they also support the value chosen for the primary zone volume in Subsection 3.2, as well as the assumption that  $V_p$  is a weak function of operating conditions. The remainder of the experiments described in this subsection were conducted without the downstream confining tube mentioned above, to allow easy photographic access. The size of the module wake region was affected by this omission, as described above, but the flow was expected to remain qualitatively the same.

A smoke generator was connected to the fuel tube to visualize the flow of a gaseous fuel. Running the test section at less than about one tenth nominal air flow, the smoke density was sufficient to see a clearly defined module wake "bubble" with smoke distributed rather evenly throughout. Downstream of this bubble the smoke was considerably less dense. These results support the assumption of a stirred-reactor primary zone which operates considerably richer than the overall fuel-air ratio, as proposed in Subsection 2.2.

An alternative technique for visualizing streaklines in the flow is the addition of helium-filled soap bubbles. A Sage Action Inc.

Model 3 bubble generator was used in a setup which paralleled the smoke visualization. The size of these bubbles could be adjusted such that they were neutrally buoyant in air, thereby following the air flow patterns with no inertial effects; this size was approximately 0.1 inch, less than 0.05 module diameter. Unfortunately, these bubbles burst rather than flow through the swirler vanes, due to the narrow passage and high shear. Therefore, bubbles were introduced into the module wake region either along the outer edge or, as shown in Figure 24, at the downstream tip along the axis. The mean air flow in this figure is from top to bottom at about one fifth nominal flow rate. Exposure time was 1/50 second, about one residence time, with forward scatter lighting such that a bubble is seen as two flares separated by one bubble diameter. In this picture, the bubbles are seen to travel "upstream" toward the swirler, then undergo looping motions indicative of the recirculation pattern, becoming involved in tight eddying motions along the way. To follow the bubble motions, high speed motion pictures at 5,000 frames per second were also taken. Projected at 16 frames per second, these movies show a module wake region full of bubbles "lazily" wandering around. There does not appear to be any organized flow pattern except for a tendency to move toward the swirler when a bubble is near the axis, and away from the swirler when near the outer edge of the module wake region. One is reminded of a random-walk process. There is never a coherent motion of a significant number of bubbles, or any evidence of large eddy shedding. When viewing the experiment



directly, the eye integrates these motions into a vibrating toroidal vortex. This helium-filled soap bubble experiment gives additional support to treating the primary zone as a stirred reactor.

To visualize the fuel droplet processes in the extreme limit of a nonevaporating fuel, a set of experiments was conducted in which water was introduced through the fuel tube. Figure 25 is a 1/20 second exposure at about one half nominal air flow rate, with a water-air ratio of 0.027 (comparable to the take-off fuel-air ratio of an engine). The air flow is from right to left. One can see the water drops coming out of the swirler and flowing outward as they move downstream; the details are out of focus except near the bottom of the picture. These droplets appear to be following an air flow pattern similar to the streamlines predicted in Section 6. Note, however, that the droplets do not turn back inward as those streamlines would predict. Apparently, the inertia of the water droplets carries them across the air streamlines into the annular air jet which comes around the blockage plate. This jet shatters the droplets down to a smaller size which is difficult to follow photographically. These droplet processes were confirmed by stroboscopic pictures using a 3 microsecond flash, and also with motion pictures taken at 5,000 frames per second. The movies enable one to follow individual droplets from frame to frame as they go through the processes described above. The process by which the droplets are formed coming out of the swirler was studied by stroboscopic close-up pictures such as Figure 26, taken at nominal air flow and a water-air ratio of 0.035.



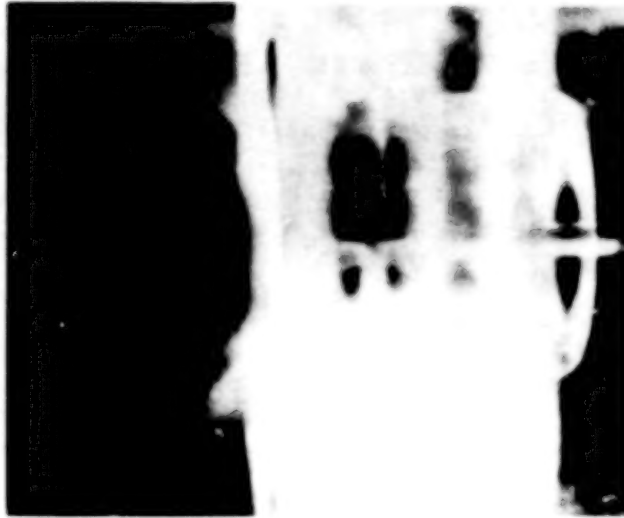


Figure 25. Streaklines of Water Droplets in Module Wake; flow is from right to left; water is injected behind swirler.

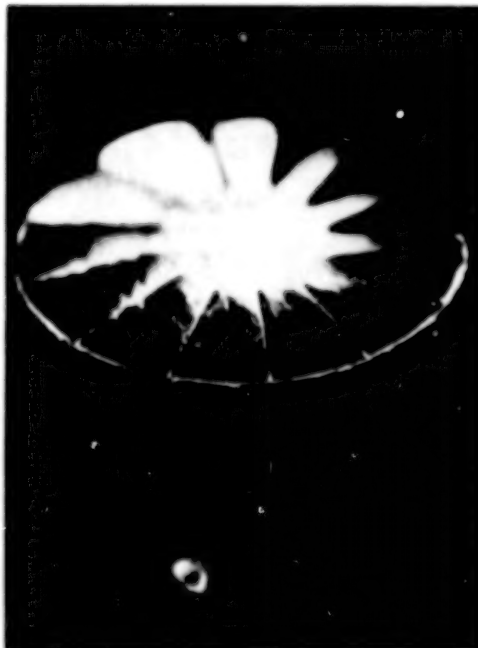


Figure 26. Closeup of Water Emerging from Swirler; water is injected behind swirler at center of hub.

Here can be seen sheets of water on the swirler vanes, ligaments being torn off, and droplets in various stages of development.

All of the water experiments thus far described were photographed using forward scatter lighting. It is difficult to obtain quantitative information about droplet sizes from this method because of the lens-like behavior of the water drops. So a series of shadowgraph pictures were taken by lining up the strobe light, a Fresnel lens, the field of droplets, and the camera along the same optical axis. Similar techniques have been described by Frazer and Dombrowski (23). Figure 27 is a shadowgraph picture taken parallel to the blockage plate at nominal air flow with a water-air ratio of 0.039. Air flow is from top to bottom, and only the left side of the flow field is shown. Measurements from photos such as this one demonstrate the effect of reference velocity on droplet size. Data are presented in Table 7, along with predictions following Prandtl, equation (27), and Wigg (24). The Prandtl equation apparently predicts an intermediate droplet size, and was therefore used to estimate initial droplet sizes for the evaporation calculations presented in Section 7. The Wigg correlation is in poor agreement with measured droplet sizes, having been developed for more conventional fuel injectors.

A final set of visualization experiments were carried out under burning conditions. For these, the downstream face of the plexiglass flange in which the module was mounted needed to be insulated from the combustion. A 1/4 inch thick transite sheet was fashioned with a hole to match the plexiglass flange hole. The assembly was

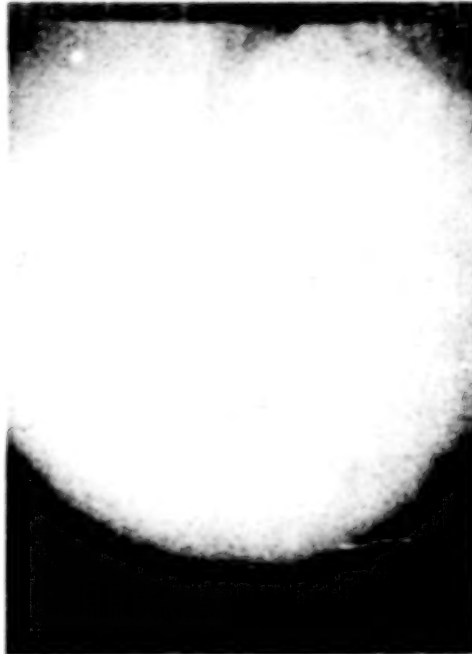


Figure 27. Shadowgraph of Water Droplets in Module Wake; flow is from top to bottom; only left side of flow field is shown

TABLE 7

Measured and Predicted Droplet Sizes

air reference velocity, m/sec	13.5	19.2	38.4
representative drop measurements, $\mu$			
near swirler	850	470	90
far downstream	240	120	mist
predicted drop sizes, $\mu$			
Prandtl, equation (27)	440	219	54
Wigg (24)	82	58	29

mounted on top of an existing vertical chimney more than one foot square in internal dimensions. Burning experiments were conducted using propane (gas) and pentane (liquid) fuels, at reference velocities and equivalence ratios typical of take-off and idle conditions. Figure 28 shows the combustion of propane at an equivalence ratio of 0.21 (approximately idle), for a reference velocity about 40% of idle conditions. The exposure time was 1/50 second, using illumination from the flame only. Flow is again from top to bottom. A roughly annular luminous region can be seen extending from the swirler about one module diameter downstream. It is a blue flame. Behind the flame are two light bands with a dark band between them, these are the edge of the hole in the transite sheet which protects the plexiglass flange, and defines the outer limit of the annular air jet. The visible flame was similar for higher reference velocities, becoming longer when operating richer. The burning of pentane did not visibly differ from the propane results described above, except that at low air flow rates a flickering yellow flame could be seen near the burner axis, immediately downstream of the swirler. This secondary flame was attributed to the large droplets of pentane which can exist at low air velocities [see equation (27)]. However, even under simulated take-off conditions, with  $\phi \approx 0.4$  some pentane droplets did escape from the combustion zone. These droplets were made visible by the two stroboscopic techniques described above, shadowgraph and forward scatter lighting. An example of the latter method is presented as Figure 29, which shows the right side of a



Figure 28. Combustion of Propane in Module Wake; overall equivalence ratio = 0.21; flow is from top to bottom, fuel is injected behind swirler



Figure 29. Combustion of Pentane in Module Wake with Droplets Escaping; overall equivalence ratio = 0.41; flow is from top to bottom, fuel is injected behind swirler; droplets illuminated by strobe light

top to bottom flow field. The lens open time for this picture was  $1/200$  second, forming an image of the blue flame at the right side where the annulus is tangent to the line of sight, thus producing the greatest intensity of light. While the lens was open, a 3 microsecond flash illuminated the pentane droplets, freezing their motion. Although it seems that a significant amount of fuel might be escaping combustion, in the full NASA combustor there would be an adjacent module wake to assist in the burning of these stray droplets; in addition, droplets would vaporize much more readily in full NASA combustor, as demonstrated in Section 7.

The visualization experiments qualitatively confirmed many of the simplifying assumptions about the flow field which were made in Subsection 3.2.

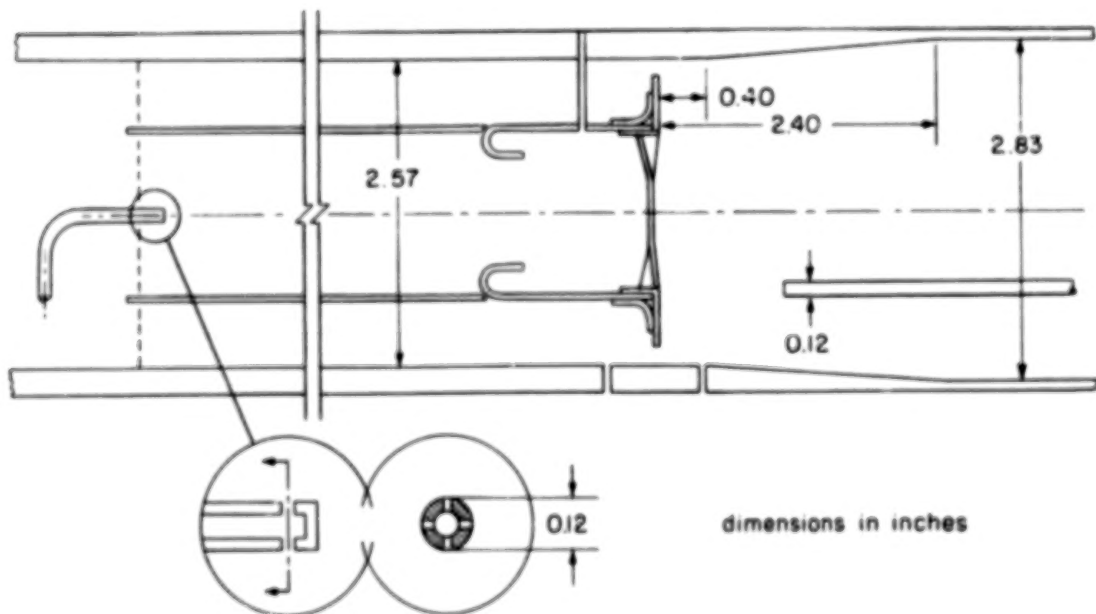


Figure 30. Diagram of Test Section for Cold Flow Tracer Experiments; flow is from left to right

## 9. Nonburning Tracer Measurements

### 9.1 Flow hardware and sample probe

Quantitative data about the flow in the NASA combustor was obtained by taking pressure measurements and cold flow tracer gas samples from a single-module test section, shown in Figure 30. The flow areas of the axisymmetric test section are an idealization of the flow areas existing in the full annular combustor liner, divided by the number of modules. Thus, there is a constant diameter section upstream of the module, extending about 0.2 module diameter downstream, a  $15^\circ$  included angle conical expansion for about one diameter, and then a constant diameter to the end of the test section. A blockage plate and standard swirler as described in Subsection 8.1 were silver soldered to a standard can body, which was supported in the test section by three radial struts.

To achieve more spatial uniformity of tracer upstream of the swirler, a tube was attached to the can body extending it about six can diameters upstream. Just past the entrance to this extension tube a coarse-mesh screen was installed to support the tracer tube and increase mixing. The tracer was injected from a point on the axis immediately downstream of this screen, discharging through four radial holes, and boosted with compressed air. This additional air was less than five percent of the estimated flow through the extension tube.

The test section exhausted into a large pipe tee and then down

into the building exhaust trench. This arrangement provided access for a straight gas sampling probe to extend into the test section, parallel to the axis. Expressed as blockage plate diameters, the probe consisted of about 3d of 0.06d tubing, flowing into an 0.2d tube which extended beyond the test section. The probe was mounted on a three-dimensional traversing mechanism such that any point of the downstream flow field could be sampled.

Propane was used in low concentrations as the tracer gas. The gas sample from the probe was passed through a Beckman Model 400 FID hydrocarbon analyzer. Sample flow rate could be varied and was found to have little effect on the relative tracer concentrations which were observed.

Pressure taps were installed to monitor pressure inside the can body and upstream and downstream of the blockage plate. An upstream total pressure probe was installed when the tracer tube and can extension tube were not in place.

## 9.2 Technique and results

The pressure measurements obtained from the locations described above were used to calculate that approximately 19 percent of the air flow passes through the can body. This calculation was derived from compressible flow relationships and the known areas, assuming isentropic flow upstream of the blockage plate and swirler. The open area of the swirler is 21 percent of the total open area in the plane of the blockage plate. This indicates that the initial velocities



of the swirler jets and annular air jet are nearly equal.

With the extension tube and tracer tube in place, gas samples were withdrawn from the flow field at several axial stations downstream of the blockage plate. After determining that the tracer concentrations were symmetric, the probing was restricted to one quadrant of the test section. Probing was done on a "grid point" basis. The grid was as fine as 0.050 x 0.100 inch (0.022 x 0.045 blockage plate diameter), depending upon the steepness of concentration gradients.

A three-dimensional representation of the tracer concentrations measured at 0.045 diameters downstream of the blockage plate is presented in Figure 31. The two axes at the left of this figure correspond to the orthogonal radii which bounded the probed quadrant. The axis extending to the right corresponds to the axis of the test section; distance along this axis represents tracer concentration. The flat region near the axis has a concentration equal to the overall tracer to air ratio. Further out one sees two complete and two partial concentration peaks which represent the rich jets coming from the swirler; since there are twelve vanes in the complete swirler, three jets can be expected in each quadrant. Maximum concentrations are about seven times the overall level, roughly corresponding to the flow split estimate described earlier. Beyond the peaks can be seen an outer plateau where concentrations are between three and four times the overall value; this represents the relatively stagnant region immediately downstream of the blockage plate (see the streamlines of Figure 22), where fuel and air have

been mixed and a flame may be stabilized. The combustion observations described in Subsection 8.2 support this location of a stabilization region.

A more quantitative presentation of the tracer concentrations can be had from the contour maps of Figure 32. These maps correspond to axial stations at 0.0045, 0.045, 0.09, 0.18, and 0.45 diameters downstream of the blockage plate. Each map represents one quadrant of the flow field, viewed from downstream. The test section axis is at the upper left, with orthogonal radii running along the top and left edges. The arc running from upper right to lower left lies slightly inside the test section wall; tracer concentrations outside this arc are essentially zero. Each boundary between a shaded and an unshaded region is a contour line (constant tracer concentration). Within each map the contour interval is one tenth of the maximum concentration at that axial station. These maxima are 7.0, 6.2, 4.9, 3.1, and 1.5 times the overall for the five maps. In each map, the region nearest the axis (upper left) is at the overall concentration; concentrations increase with radius, passing through the rich jet region, then decreasing toward zero as the test section wall is approached. The jet structure is clearly defined in the first few maps, becoming more diffuse and merging circumferentially as the flow progresses downstream. A small amount of counter-clockwise swirl is also apparent. By 0.9 diameter downstream of the blockage plate, the tracer concentration is quite uniform across the test section. Decreasing the reference velocity by a factor of four

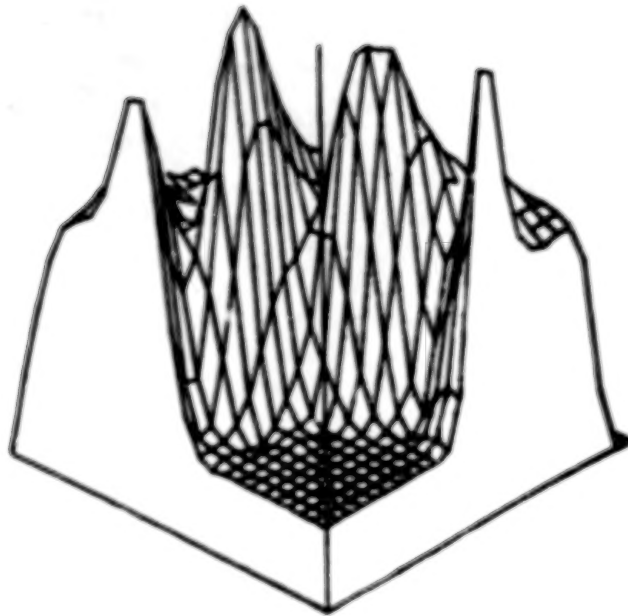


Figure 31. Three Dimensions: Plot of Tracer Concentration; at One Axial Station; axes at left define probed quadrant, distance along horizontal axis represents tracer concentration



Figure 32a. Contour Map of Tracer Concentrations at 0.0045 Module Diameter Downstream; test section axis is at upper left, quadrant viewed looking upstream



Figure 32b. Contour Map of Tracer Concentrations at 0.045 Module Diameter Downstream; test section axis is at upper left, quadrant viewed looking upstream



Figure 32c.. Contour Map of Tracer Concentration at 0.09 Module Diameter Downstream; test section axis is at upper left, quadrant viewed looking upstream

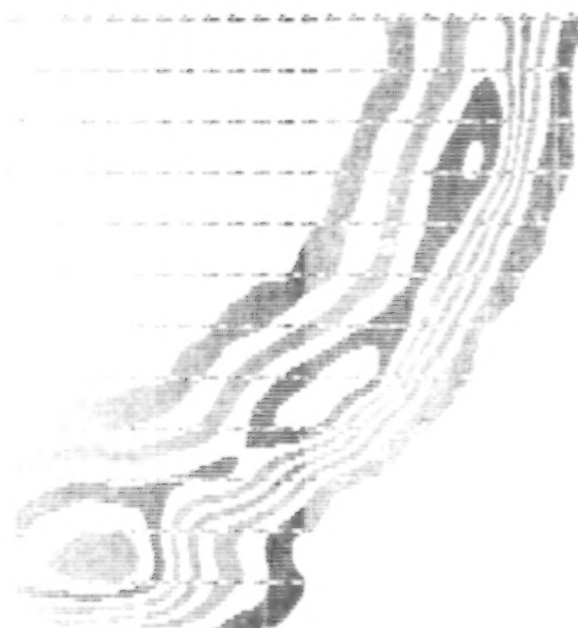


Figure 32d. Contour Map of Tracer Concentrations at 0.18 Module Diameter Downstream; test section axis is at upper left, quadrant viewed looking upstream

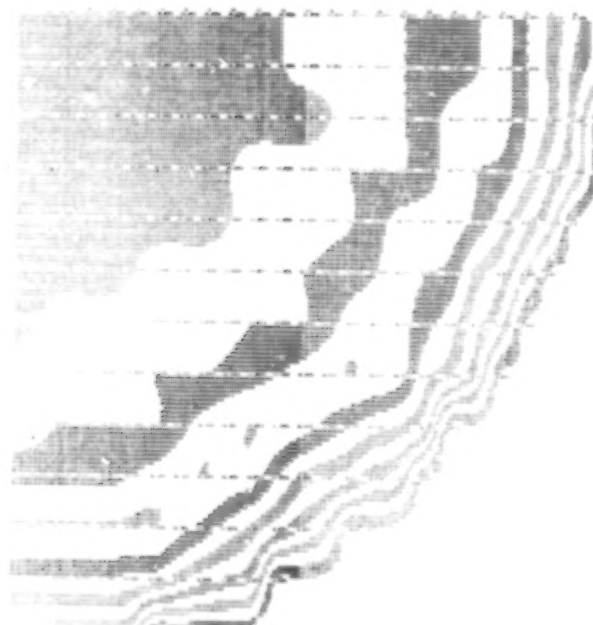


Figure 32e. Contour Map of Tracer Concentrations at 0.45 Module Diameter Downstream; test section axis is at upper left, quadrant viewed looking upstream

did not noticeably alter these contour maps, thus confirming the lack of Reynolds number effect predicted in Section 6.

The swirler jets can be quantitatively followed as they progress downstream, moving outward and entraining surrounding gases. A radial line drawn through the concentration peak of a jet at each axial station produces a cross-section representative of the jet structure. A number of these jet cross-sections are shown in Figure 33, where tracer concentrations are plotted against radius. The jets can clearly be seen to move outward and dilute themselves with surrounding gases as they progress downstream. This process is completed by about one module diameter downstream.

A gross dilution rate for the swirler jets can be estimated by using this tracer concentration data. Following Hoult and Weil (25) an entrainment parameter may be defined as

$$\alpha = \frac{\dot{m}}{\rho A V(1 - \cos \theta)} \quad (28)$$

where  $\dot{m}$  is the mass entrainment rate,  $\rho$  is the gas density,  $A$  is the area through which mass is being entrained, and  $V(1 - \cos \theta)$  is the relative tangential velocity between the swirler jets and the annular air flow between the swirler jets and the test section wall. All dilution is attributed to tangential entrainment for the purposes of this calculation. Let  $d_p$  be the blockage plate diameter and  $d_0$  be the test section diameter at the blockage plate axial station. If the swirler jets entrain all of the annular air flow, one may write

$$\dot{m} = \frac{\pi}{4} \rho V(d_o^2 - d_p^2) \quad (29)$$

If the entrainment occurs in an axial distance equal to the blockage plate diameter, the entrainment area may be approximated as

$$A \sim \frac{\pi d_p^2}{\cos \theta} \quad (30)$$

Substituting equations (29) and (30) into equation (28), one obtains

$$\alpha \sim \frac{(d_o^2 - d_p^2) \cos \theta}{4d_p^2(1 - \cos \theta)} \quad (31)$$

Using a value of  $\theta \sim 60^\circ$  obtained from Figure 33 and plugging in the values of  $d_o$  and  $d_p$ , one obtains a value of  $\alpha \sim 0.08$ . This crude estimate agrees surprisingly well with the value 0.078 ( $\approx 0.11/\sqrt{2}$ ) reported by Hoult and Weil (25) for Gaussian velocity profiles.

Cold flow data presented in this section generally support the flow calculations of Section 6. Additions have also been made to the qualitative understanding of the flow field, particularly the region within one diameter of the blockage plate. A quantitative understanding of the flow field under combustion conditions will be developed in the next section.

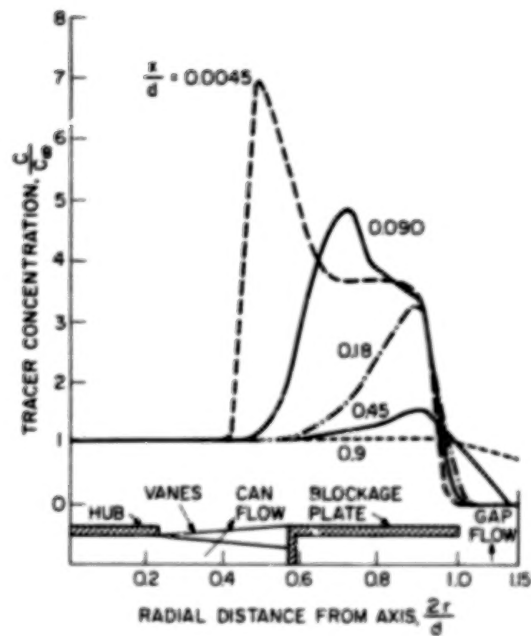


Figure 33. Tracer Concentration versus Radius at Various Axial Stations; radius runs through swirler jet concentration peak at each station

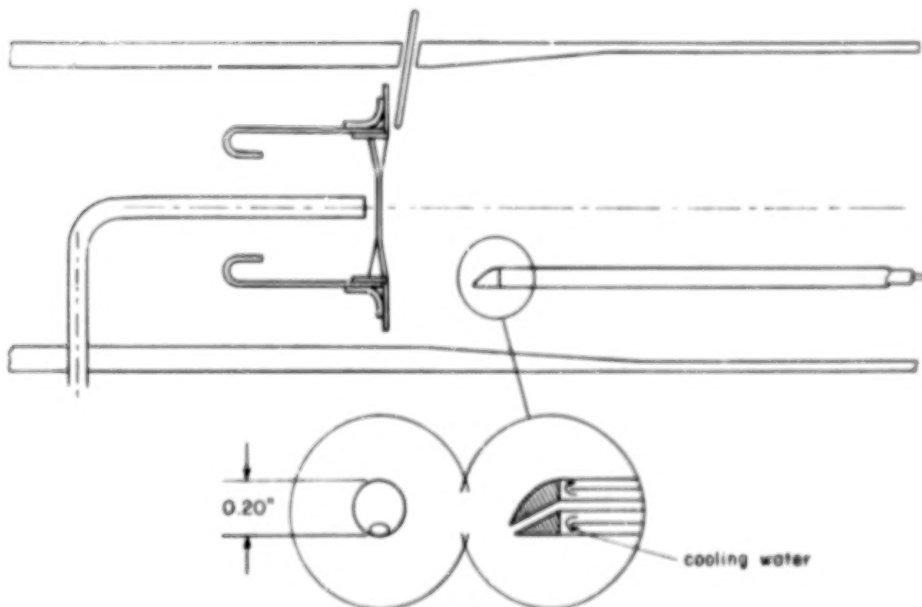


Figure 34. Diagram of Test Section and Probe for Gas Sampling under Burning Conditions; a modification of the cold flow tracer section (Figure 30); flow is from left to right



## 10. Measurements under Burning Conditions

### 10.1 Flow hardware and sample probe

The measurements taken under burning conditions were done in the same test section as the cold-flow tracer experiments, as described in Subsection 9.1, with the following changes (see Figure 34):

The upstream extension tube was removed from the swirl-can. The tracer injector was replaced by a fuel tube which simulated NASA's design, a 3/16 inch tube running along the axis of the test section to a point 1/8 inch upstream of the swirler, terminating in an 0.052 inch orifice. A single-electrode igniter was added immediately downstream of the blockage plate, at the top of the test section such that the spark would arc between the igniter and the blockage plate.

Copper tubing was wrapped around the outside of the test section for cooling water. A spray bar was installed inside the exhaust tee, downstream of the test section, for water-cooling the walls of the tee. A spray-cooled deflection plate was installed in the building exhaust trench below the exhaust tee.

A water-cooled sample probe was constructed of three concentric stainless steel tubes, with a skewed copper tip. Mounted on the three-dimensional traversing mechanism, the probe passed through the exhaust tee, extending into the test section parallel to the axis. The portion of the probe which extended into the test section had a diameter of 0.20 inch, which is 0.09 times the blockage plate diameter. The probe tip (see Figure 34) was contoured to provide an aerodynamically smooth transition from the concentric tubes to the

sample inlet. This inlet was located approximately one probe diameter beyond the end of the concentric tubes, offset from the probe's axis by one radius. Thus, the probe could be used to sample right up to the wall of the test section without excessively disturbing the flow field.

## 10.2 Choice of propane fuel

As described in Section 7, it was determined that pentane fuel would have a longer evaporation distance for ambient inlet air conditions than kerosene has under typical engine operating conditions. Gaseous propane fuel would simulate the instantaneous evaporation of a liquid fuel. A comparison of the combustion of pentane and propane could confirm the argument of Section 7 that droplet evaporation effects are not significant in the NASA swirl-can combustor.

When the experimental burner was operated on pentane, it was found that a significant portion of the fuel would reach the relatively cool wall of the test section without evaporating. This liquid fuel flowed downstream along the wall to the end of the test section, where the hot gases dump into the exhaust tee. At this point a secondary flame was attached, burning inside the exhaust tee. While this situation was an interesting combustion phenomenon, it could not simulate the combustion downstream of the 120-module NASA swirl-can array. That is, a solid wall cannot simulate imaginary surfaces of flow symmetry under conditions where fuel droplets

impinge upon that wall. It was decided to proceed with combustion experiments using gaseous propane fuel to approximate the rapid evaporation of kerosene expected under engine operating conditions.

### 10.3 Gas sample analysis hardware

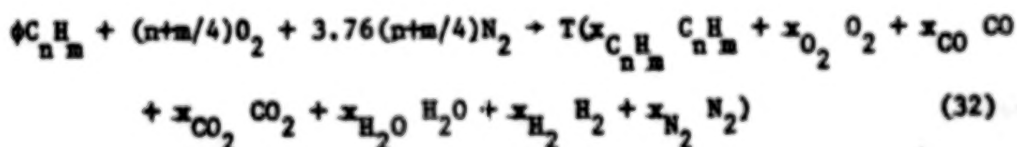
The gas samples drawn through the probe described in Subsection 10.1 were pulled through a length of unheated plastic tubing into a diaphragm pump, then through an ice-bath moisture trap followed by desiccant tubes, and into the continuous-reading instrumentation. These instruments were: a Beckman Model 315A NDIR for  $\text{CO}_2$ , Beckman Models 315A and 864 NDIR's for CO, a Scott Model 150 paramagnetic for  $\text{O}_2$ , a Scott Model 215 FID for total hydrocarbons (HC), and a Thermo-Electron Model 10A chemiluminescent for  $\text{NO}_x$ . For a sample with more than 100,000 ppm HC (as  $\text{C}_1$ ), the sample was diluted with nitrogen in order to bring it within the range of the HC instrument. Since the  $\text{NO}_x$  readings were always less than 50 ppm, it was treated as a minor species whose magnitude did not affect the calculated values of local equivalence ratio and mixture nonuniformity which were evaluated in the combustion experiments.

### 10.4 Reduction of data to local equivalence ratio

When a gas sample is taken from a point in the test section, the gas analysis instrumentation described in the previous subsection provides time-average measurements of mole fractions of  $\text{CO}_2$ , CO and

$O_2$  and mole fraction times average carbon number for hydrocarbons, all on a dry basis. This information alone is not sufficient for the determination of local equivalence ratio, unless some assumptions are made. Many of the published methods for calculating equivalence ratio, such as the Spindt method (26), rely on a "water-gas" equilibrium constant. This assumes that  $H_2O$  and  $CO$  are in a quasi-equilibrium with  $CO_2$  and  $H_2$ . While this assumption may be reasonably accurate for piston engine exhaust gases, it is unlikely to be valid for gas samples drawn from arbitrary points in a complex combustor flow field. An alternative assumption was therefore developed.

For a combustor fueled by a light stable hydrocarbon such as propane, it may be assumed that the hydrocarbon to which the hydrocarbon analyzer is responding is the same as the fuel which is fed into the combustor. The justification for this assumption is that in regions where hydrocarbon concentrations are high, the fuel is likely to be nearly unburned and unreacted; in regions of low hydrocarbon concentration it is a minor species and the assumption has little effect on the equivalence ratio. For the hydrocarbon fuel  $C_n H_m$ , the average reaction for gases sampled at a point in the flow field may be written for major species as



where  $\phi$  is the equivalence ratio,  $T$  is the number of moles of products and  $x_i$  is mole fraction of species  $i$ . Balance equations may be written for C, H, O, and  $N_2$  as follows:

$$n\phi = T(nx_{C_nH_m} + x_{CO} + x_{CO_2}) \quad (33)$$

$$m\phi = T(mx_{C_nH_m} + 2x_{H_2O} + 2x_{H_2}) \quad (34)$$

$$2(n + m/4) = T(2x_{O_2} + x_{CO} + 2x_{CO_2} + x_{H_2O}) \quad (35)$$

$$3.76(n + m/4) = T x_{N_2} \quad (36)$$

The four dry basis species measurements may be equated to  $x_{CO_2}/(1-x_{H_2O})$ ,  $x_{CO}/(1-x_{H_2O})$ ,  $x_{O_2}/(1-x_{H_2O})$ , and  $n x_{C_nH_m}/(1-x_{H_2O})$ . It is also known that the mole fractions on the right-hand side of reaction (32) sum to unity. Thus there are nine equations written in terms of  $n$ ,  $m$ ,  $\phi$ ,  $T$ , and the seven mole fractions,  $x_i$ . For a given fuel  $n$  and  $m$  may be determined, and the system of equation may then be solved. In particular, the equations may be written in terms of the unknowns  $\phi$ ,  $T$ , and  $T x_i$ , resulting in linear equations.

The method described above was applied to data obtained from the test section described in Subsection 10.1, burning  $C_3H_8$ . The resulting equivalence ratios and mole fractions seemed reasonable, except that for about one-third of the data  $x_{H_2}$  was negative by a few percent (in rare instances  $x_{H_2O}$  was negative). This was

attributed to a relatively minor species being quite sensitive to inaccuracies in the gas analysis data. The calculated equivalence ratios were much less sensitive.

In order to compensate for these measurement errors, a method was devised to solve the system of equations in a least squares sense with respect to the measurements, constraining  $x_{H_2}$  and  $x_{H_2O}$  to be non-negative. The method was built around an available routine for the minimization of a sum of squares. The equations were solved for the remaining variables in terms of  $x_{H_2}$ ,  $x_{H_2O}$ ,  $\phi$ , and  $T$ . The minimization routine searched over these four variables; at each point a feasible solution (for the  $x_i$ ) was calculated. An objective function could then be expressed as

$$\sum_i \left[ \frac{\bar{R}_i (1 - x_{H_2O,c})}{x_{i,c}} - 1 \right]^2 \quad (37)$$

where  $R_i$  is the species  $i$  measurement expressed as a dry basis mole fraction (dividing by  $n$  in the case of hydrocarbons), and the subscript  $c$  refers to calculated values. The minimization routine directed the search such that expression (37) was minimized. The point at which this occurred was taken to be the best fit to experimental data. Equivalence ratios resulting from this method will be used in this section.

### 10.5 Reduction of data to local nonuniformity parameter

Burner gas sample concentrations may also be used to generate a measure of the mixture nonuniformity at the point where the sample is taken. Assume that the sample probe pulls in a rapid succession of discrete packets of various fuel fractions, and that each packet is completely homogeneous. Further assume that each packet is in the chemical equilibrium corresponding to its fuel fraction, the inlet air temperature, and the fuel properties, i.e. combustion is complete with no net heat transfer. Flammability limits may be imposed upon this assumption; for the calculations presented herein they were arbitrarily set at  $\phi=0$  and  $\phi=3$ , wide enough not to significantly affect the results. If the fuel fractions of these packets are distributed according to equation (15), average mole fractions of  $\text{CO}_2$ ,  $\text{CO}$ ,  $\text{O}_2$ , and  $\text{H}_2\text{O}$  for the mixture may be obtained by calculating equilibrium moles of each species per unit mass, for a range of fuel fractions, then weighting these on a mass basis using equation (15). Average mole fractions of  $\text{CO}_2$ ,  $\text{CO}$ , and  $\text{O}_2$  on a dry basis may in turn be computed; these are what would be measured on the gas analysis setup described in subsection 10.3 where the packets would be quenched, mixed, and desiccated on their way through the flow system.

The only unknowns in the calculations described above are the variables  $\bar{F}$  and  $\sigma$  in equation (15). Given a set of gas sample measurements,  $\bar{F}$  is best computed from the equivalence ratio method of the previous subsection. The sum of squares minimization routine was then used to search over the variable  $\sigma$ ; for each value, a



feasible set of dry-basis  $\text{CO}_2$ ,  $\text{CO}$ , and  $\text{O}_2$  mole fractions was generated as described above. An objective function was then calculated as

$$\sum_{i=1}^I \left[ \frac{\bar{R}_i}{R_{i,c}} - 1 \right]^2 \quad (38)$$

using the notation of expression (37). Hydrocarbons were not included in expression (38) because they would be sensitive to the choice of realistic flammability limits. The minimization routine then directed the search over  $\sigma$  such that expression (38) was minimized. The point at which this occurred was taken to be the best fit to the experimental data, given all the assumptions made earlier in this subsection. Values of the mixing parameter  $s$  could then be calculated using equation (16); these will be presented in the next subsection.

The assumptions upon which this subsection is based are equivalent to the corresponding assumptions which were made in Subsections 2.1 and 2.2 for the calculation of  $\text{NO}_x$ ; the  $s$  parameter values which are thereby calculated are the correct ones to compare with  $s$  values which enter into the  $\text{NO}_x$  predictions. To the extent that the assumptions are in error, the errors will self-compensate.



## 10.6 Results

The hardware described in Subsections 10.1 and 10.3 was used to obtain local species concentrations while propane was being burned in the test section. After determining that the flow field was roughly symmetric in terms of these concentrations, detailed probing was conducted in a single quadrant. A grid-point system as fine as  $0.100 \times 0.100$  inch ( $0.045 \times 0.045$  blockage plate diameter) was used, depending upon the steepness of concentration gradients. Full quadrants were probed at 0.22, 0.45, and 0.90 diameter downstream of the blockage plate, for a reference velocity of 23 m/s (75 ft/s), at an overall equivalence ratio of approximately 0.4. Concentration data thus obtained were reduced to grid-point values of equivalence ratio  $\phi$  and mixing parameter  $s$ , using the methods described in Subsections 10.4 and 10.5.

Equivalence ratio contour maps (similar to the maps of Figure 32 described in Subsection 9.2) are presented in Figure 35. The contour interval for all of these maps is 0.2  $\phi$  unit. The unshaded region in the upper left of each of these maps (closest to the test section axis) is the contour band  $0.6 < \phi < 0.8$ , or 1.5 to 2.0 times the overall  $\phi$ . In Figure 35a  $\phi$  increases with radius to a maximum of 2.1 in a region where some rich jet structure is visible; beyond this,  $\phi$  decreases toward a value of zero near the test section wall (the annular air jet). Figure 35b shows  $\phi$  increasing with a radius to a region of  $0.8 < \phi < 1.0$ , with a pocket of  $\phi$



Figure 35a. Contour Map of Equivalence Ratio at 0.22 Module Diameter Downstream; test section axis is at upper left, quadrant viewed looking upstream



Figure 35b. Contour Map of Equivalence Ratio at 0.45 Module Diameter Downstream; test section axis is at upper left, quadrant viewed looking upstream

# TABLE OF CONTENTS

		Page	
CHAPTER 1	INTRODUCTION . . . . .	1	1/A10
CHAPTER 2	MODEL DESCRIPTION . . . . .	5	1/A14
	2.1 Chemical Kinetics of NO <sub>x</sub> formation . . . . .	5	1/A14
	2.2 Effects of fuel-air nonuniformities; a primary zone model . . . . .	13	1/B8
	2.3 A multi-zone flow model with Monte Carlo mixing. . . . .	21	1/C2
CHAPTER 3	COMPARISONS OF NO <sub>x</sub> PREDICTIONS WITH AVAILABLE EXPERIMENTAL DATA . . . . .	24	1/C5
	3.1 A 'premixed' tubular burner. . . . .	24	1/C5
	3.2 The NASA swirl-can modular combustor . . . . .	28	1/C9
CHAPTER 4	OPERATING CHARACTERISTICS OF THE NASA COMBUSTOR INFERRED FROM NO <sub>x</sub> DATA . . . . .	43	1/D10
CHAPTER 5	PARAMETRIC STUDIES. . . . .	45	1/D12
CHAPTER 6	AIR FLOW STREAMLINE CALCULATIONS. . . . .	53	1/E6
CHAPTER 7	CALCULATION OF FUEL DROPLET EVAPORATION . . . . .	56	1/E9
CHAPTER 8	FLOW VISUALIZATION EXPERIMENTS. . . . .	59	1/E12
	8.1 Flow hardware. . . . .	59	1/E12
	8.2 Techniques and Results . . . . .	61	1/E14
CHAPTER 9	NONBURNING TRACER MEASUREMENTS. . . . .	70	1/F9
	9.1 Flow hardware and sample probe . . . . .	70	1/F9
	9.2 Technique and results. . . . .	71	1/F10
CHAPTER 10	MEASUREMENTS UNDER BURNING CONDITIONS . . . . .	80	1/G5
	10.1 Flow hardware and sample probe. . . . .	80	1/G5
	10.2 Choice of propane fuel. . . . .	81	1/G6
	10.3 Gas sample analysis hardware. . . . .	82	1/G7
	10.4 Reduction of data to local equivalence ratio. . . . .	82	1/G7
	10.5 Reduction of data to local nonuniformity parameter. . . . .	86	1/G11
	10.6 Results . . . . .	88	1/G13
CHAPTER 11	SUMMARY AND CONCLUSIONS . . . . .	94	2/A11
REFERENCES	. . . . .	96	2/A13

# LIST OF FIGURES

<u>Figure</u>		<u>Page</u>
1.	NO versus Time for Stoichiometric Burned Gas at Various Temperatures; pressure = 15 atm; fuel=kerosene; dashed lines are equilibrium levels from Heywood, et. al. (11) . . . . .	12 1/B7
2.	Characteristic Time for NO Formation versus Equivalence Ratio for Various Engine Pressure Ratios; see Table 3 for inlet conditions. . . . .	12 1/B7
3.	Rate of Increase in NO <sub>x</sub> Emission Index versus Mean Equivalence Ratio for Various Values of Nonuniformity Parameter, 8:1 Engine Pressure Ratio; see Table 3 for inlet conditions. . . . .	14 1/B9
4.	Rate of Increase in NO <sub>x</sub> Emission Index versus Mean Equivalence Ratio for Various Values of Nonuniformity Parameter, 16:1 Engine Pressure Ratio; see Table 3 for inlet conditions. . . . .	18 1/B13
5.	Rate of Increase in NO <sub>x</sub> Emission Index versus Mean Equivalence Ratio for Various Values of Nonuniformity Parameter, 24:1 Engine Pressure Ratio; see Table 3 for inlet conditions. . . . .	18 1/B19
6.	Rate of Increase in NO <sub>x</sub> Emission Index versus Mean Equivalence Ratio for Various Values of Nonuniformity Parameter, 32:1 Engine Pressure Ratio; note NO <sub>x</sub> scale shift from previous figures; see Table 3 for inlet conditions . . . . .	19 1/B19
7.	Comparison of NO <sub>x</sub> Predictions with Premixed Experimental Data, 800 K Inlet; pressure = 5.5 atm; s = 0 for curve A, s = 0.1 for curve B; data from Anderson (15). . . . .	26 1/C7
8.	Comparison of NO <sub>x</sub> Predictions with Premixed Experimental Data, 600 K Inlet; see text for details . . . . .	26 1/C7
9.	Details of NASA Swirl-Can Module. . . . .	30 1/C11
10.	Tangential View of NASA Swirl-Can Combustor Annulus . . . . .	30 1/C11
11.	Comparison of NO <sub>x</sub> Predictions with NASA Swirl-Can Data (4) for Various Values of a Constant Mixing Intensity (solid curves); fixed primary zone parameters. . . . .	35 1/D2
12.	Comparison of NO <sub>x</sub> Predictions with NASA Swirl-Can Data (4) for Various Values of Mixing Intensity Decay Time (solid curves); fixed primary zone and initial intensity . . . . .	35 1/D2

FigurePage

13.	Comparison of NO <sub>x</sub> Predictions with NASA Swirl-Can Data (4) for Various Initial Mixing Intensity/Decay Time Pairs (solid curves); fixed primary zone and pair product . . . . .	40	1/D7
14.	Comparison of NO <sub>x</sub> Predictions with NASA Swirl-Can Data (4) using Parameter Values Fit at Different Inlet Temperatures (solid curves). . . . .	40	1/D7
15.	NO <sub>x</sub> Predictions versus Pressure for a NASA Swirl-Can Module, Baseline Case; see text for details; circles are test rig data obtained by NASA . . . . .	44	1/D11
16.	NO <sub>x</sub> Predictions versus Pressure for a NASA Swirl-Can Module, Parametric Study; see text for details middle curve of each trio is baseline case (Figure 15) . . . . .	47	1/D14
17.	NO <sub>x</sub> Predictions versus Initial Mixing Intensity for Various Values of Primary Zone Nonuniformity, Typical Engine Conditions; see text for details . . . . .	51	1/E4
18.	NO <sub>x</sub> Predictions versus Mixing Intensity Decay Time for Various Values of Primary Zone Nonuniformity, Typical Engine Conditions; see text for details. . . . .	51	1/E4
19.	NO <sub>x</sub> Predictions versus Primary Zone Volume for Various Values of Primary Zone Enrichment Factor, Typical Engine Conditions; see text for details . . . . .	52	1/E5
20.	NO <sub>x</sub> Predictions versus Primary Zone Nonuniformity for Various Values of Primary Zone Enrichment Factor, Typical Engine Conditions; see text for details. . . . .	54	1/E7
21.	Schematic of Boundary Conditions for Numerical Flow Calculations. . . . .	54	1/E7
22.	Streamline Plot of Calculated Flow Field; flow is from top to bottom, with symmetry axis at left side . . . . .	55	1/E8
23.	Diagram of Visualization Test Section flow is from top to bottom. . . . .	60	1/E13
24.	Helium-filled Soap Bubble Traces in Module Wake; mean flow is from top to bottom; bubbles are injected at tip of recirculation zone . . . . .	60	1/E13
25.	Streaklines of Water Droplets in Module Wake; flow is from right to left; water is injected behind swirler . . . . .	64	1/F3
26.	Closeup of Water Emerging from Swirler; water is injected behind swirler at center of hub. . . . .	64	1/F3
27.	Shadowgraph of Water Droplets in Module Wake; flow is from top to bottom; only left side of flow field is shown. . . . .	66	1/F5

<u>Figure</u>		<u>Page</u>
28.	Combustion of Propane in Module Wake; overall equivalence ratio = 0.21; flow is from top to bottom, fuel is injected behind swirler . . . . .	68 1/F7
29.	Combustion of Pentane in Module Wake with Droplets Escaping; overall equivalence ratio = 0.41; flow is from top to bottom, fuel is injected behind swirler; droplets illuminated by strobe light. . . . .	68 1/F7
30.	Diagram of Test Section for Cold Flow Tracer Experiments; flow is from left to right . . . . .	69 1/F8
31.	Three Dimensional Plot of Tracer Concentrations at One Axial Station; axes at left define probed quadrant, distance along horizontal axis represents tracer concentration. . . . .	74 1/F13
32a.	Contour Map of Tracer Concentrations at 0.0045 Module Diameter Downstream; test section axis is at upper left, quadrant viewed looking upstream. . . . .	74 1/F13
32b.	Contour Map of Tracer Concentrations at 0.045 Module Diameter Downstream; test section axis is at upper left, quadrant viewed looking upstream. . . . .	75 1/F14
32c.	Contour Map of Tracer Concentration at 0.09 Module Diameter Downstream; test section axis is at upper left, quadrant viewed looking upstream. . . . .	75 1/F14
32d.	Contour Map of Tracer Concentrations at 0.18 Module Diameter Downstream; test section axis is at upper left, quadrant viewed looking upstream. . . . .	76 1/G1
32e.	Contour Map of Tracer Concentrations at 0.45 Module Diameter Downstream; test section axis is at upper left, quadrant viewed looking upstream . . . . .	76 1/G1
33.	Tracer Concentration versus Radius at Various Axial Stations; radius runs through swirler jet concentration peak at each station. . . . .	79 1/G4
34.	Diagram of Test Section and Probe for Gas Sampling under Burning Conditions; a modification of the cold flow tracer section (Figure 30); flow is from left to right. . . . .	79 1/G4
35a.	Contour Map of Equivalence Ratio at 0.22 Module Diameter Downstream; test section axis is at upper left, quadrant viewed looking upstream . . . . .	89 1/G14
35b.	Contour Map of Equivalence Ratio at 0.45 Module Diameter Downstream; test section axis is at upper left, quadrant viewed looking upstream . . . . .	89 1/G14



<u>Figure</u>		<u>Page</u>
35c.	Contour Map of Equivalence Ratio at 0.09 Module Diameter Downstream; test section axis is at upper left, quadrant viewed looking upstream. . . . .	90 2/A7
36a.	Contour Map of Nonuniformity Parameter at 0.22 Module Diameter Downstream; test section axis is at upper left, quadrant viewed looking upstream; values not meaningful in region of mottled shading. . . . .	90 2/A7
36b.	Contour Map of Nonuniformity Parameter at 0.45 Module Diameter Downstream; test section axis is at upper left, quadrant viewed looking upstream; values not meaningful in region of mottled shading. . . . .	91 2/A8
36c.	Contour Map of Nonuniformity Parameter at 0.9 Module Diameter Downstream; test section axis is at upper left, quadrant viewed looking upstream. . . . .	91 2/A8

## LIST OF TABLES

<u>Table</u>		<u>Page</u>	
1.	Rate Constants for the NO <sub>x</sub> Kinetic Reaction Scheme. . . . .	7	1/B2
2.	Typical Values for Quantities Entering into Rate Equation (11). . .	11	1/B6
3.	Inlet Temperatures and Pressures Appropriate to the NO <sub>x</sub> Time Constants and Formation Rates of Figures 2 through 6 . . . . .	14	1/B9
4.	Typical Data Appropriate to the Premixed NO <sub>x</sub> Calculations of Figure 7. . . . .	19	1/B14
5.	Data Relevant to a NO <sub>x</sub> Prediction Curve for the NASA Swirl-Can Combustor . . . . .	42	1/D9
6.	Fuel Droplet Evaporation Parameters and Calculated Results for Engine Conditions and a Simulation. . . . .	58	1/E11
7.	Measured and Predicted Droplet Sizes. . . . .	66	1/F5



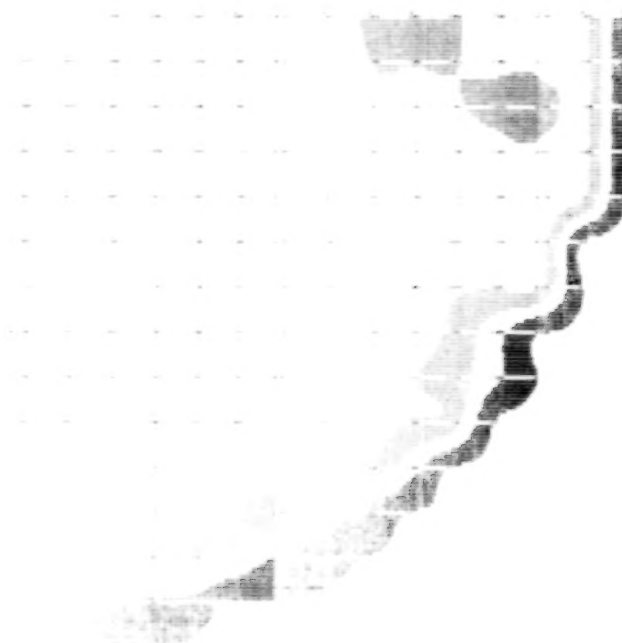


Figure 35c. Contour Map of Equivalence Ratio at 0.09 Module Diameter Downstream; test section axis is at upper left, quadrant viewed looking upstream



Figure 36a. Contour Map of Nonuniformity Parameter at 0.02 Module Diameter Downstream; test section axis is at upper left, quadrant viewed looking upstream; values not meaningful in region of mottled shading

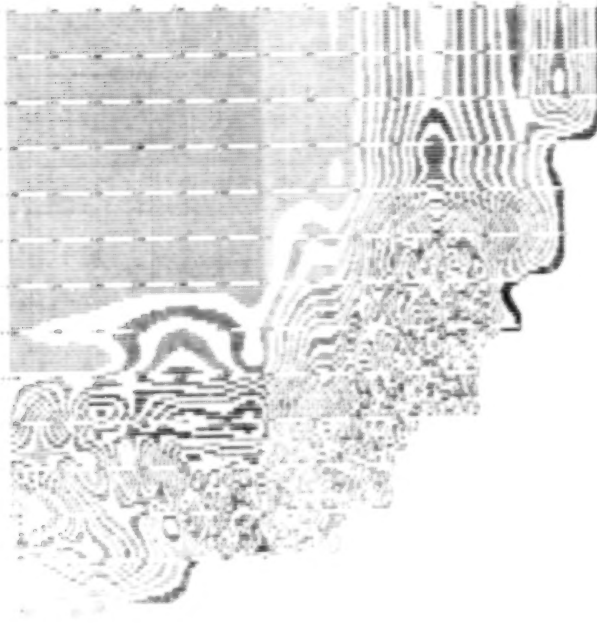


Figure 36b. Contour Map of Nonuniformity Parameter at 0.45 Module Diameter Downstream; test section axis is at upper left, quadrant viewed looking upstream; values not meaningful in region of mottled shading

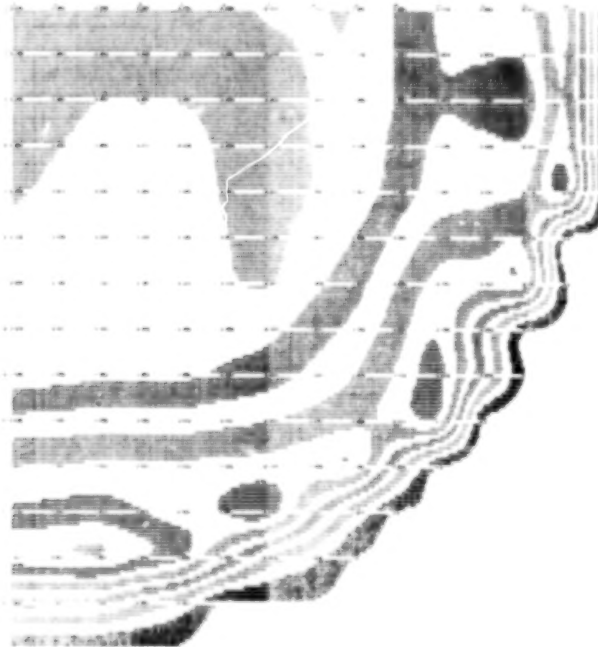


Figure 36c. Contour Map of Nonuniformity Parameter at 0.9 Module Diameter Downstream; test section axis is at upper left, quadrant viewed looking upstream

slightly greater than 1.0 at the upper right;  $\phi$  then decreases toward zero at the test section wall. In Figure 35c, except for pockets of  $\phi$  slightly greater than 0.8 at the upper right,  $\phi$  simply decreases toward zero beyond the central region.

There are significant differences between these  $\phi$  maps obtained under combustion conditions and the cold-flow tracer maps of Subsection 9.2. The region near the test section axis is considerably richer than the overall  $\phi$ , as noted above. The structure of the rich swirler jets is not nearly as well-defined or symmetric. However, the hot and cold-flow data are roughly similar in a qualitative sense.

In terms of evaluating the module wake enrichment factor  $F_p/F_o$ , a precise value cannot be obtained without weighting all the points in the wake according to their relative importance to the formation of  $NO_x$ . This would involve detailed measurements not only of  $\phi$ , but also the relative residence time at each point. The  $NO_x$  emissions data matching of Subsection 3.2 produced a value of 2.5. For the contour maps of Figure 35, this corresponds to  $\phi \sim 1.0$ . Generally it is seen that  $0.7 \lesssim \phi \lesssim 1.5$ . There are extensive regions of Figure 35b where  $\phi$  is near unity. Upstream of these regions (Figure 35a)  $\phi$  is higher, and downstream (Figure 35c)  $\phi$  is lower. Thus, in a rough sense, support is given to the approximation  $F_p/F_o \sim 2.5$ .

Contour maps of mixing parameter (for the same axial stations as the  $\phi$  maps) are shown in Figure 36. For all of the  $s$  maps the

contour interval is 0.1  $s$  unit. The shaded region in the upper left of each of these regions is the contour band  $0.2 < s < 0.3$ . In Figure 36a there are patches where  $s$  is slightly less than 0.2, a couple of peaks which are suspected to be bad data points, then a sharp increase of  $s$  with radius to calculated values well above unity, which appear as random shading. These high values are not considered meaningful since the assumptions of Subsection 10.5 will not be valid in these regions. In regions where pure air is found,  $s$  will be undefined because the local fuel fraction is zero; for the purposes of Figure 36,  $s$  has been constrained to be zero at the test section wall. Figure 36b shows a more constant value of  $s$  at the upper left, with a more gradual increase to  $s \gg 1$ . In Figure 36c, the  $s$  values are quite well behaved, increasing with radius toward three or four peaks where  $0.8 < s < 1.0$ ; beyond this,  $s$  decreases toward the  $s=0$  constraint at the wall. These peaks seem to be vestiges of the swirler jet structure, information which was not visible in the corresponding  $\phi$  map (Figure 35c).

As in the case of the parameter  $F_p/F_o$  it is not possible to obtain a precise value for the appropriate average module-wake mixing parameter  $s_p$ . The  $\text{NO}_x$  emissions data matching of Subsection 3.2 produced a value of 0.4. Generally it is seen that  $0.25 \lesssim s < 1+$ . There is a wide region where  $0.3 < s < 0.5$  in Figure 36c, although it is weighted toward a smaller test section radius than the regions of Figure 35 where  $\phi \sim 1$ . Upstream, in Figures 36 b and a, the region

$s \sim 0.4$  is narrower. Thus, the  $s$  maps tend to support the approximation  $s_p \approx 0.4$ .

## 11. Summary and Conclusions

This report has presented a model for predicting  $\text{NO}_x$  emissions from gas turbine combustors. The structure of the model is modular, and is not restricted to particular combustor geometries. It consists of a stirred reactor followed by plug flow reactors to which dilution air can be added. A modified Zeldovich scheme is used for the  $\text{NO}$  formation kinetics. Fuel-air nonuniformities are incorporated. Application of this model to a tubular premixed combustor, and the NASA swirl can combustor produced quite satisfactory agreement with available emissions measurements. Numerical calculations of streamlines and fuel evaporation backed up the application of the model to the NASA swirl-can combustor. Visualization experiments were also conducted for better understanding. Confirming quantitative data came from experiments with cold-flow tracer and propane-burning gas sampling. A general model for  $\text{NO}_x$  formation such as the one described herein, supported by theoretical calculations and experiments, can be useful for the interpolation and extrapolation of test data, for examining the effects of design trade-offs, and for increasing the understanding of processes inside a gas turbine combustor.

The major general conclusions are:

- (1) A modified Zeldovich kinetic scheme using equilibrium combustion products is sufficient for the calculation of  $\text{NO}_x$  formation under typical gas turbine conditions.

- (2) The type of general  $\text{NO}_x$  model presented herein can extract information about entrainment and mixing in the combustor from engine emission data.
- (3) Low  $\text{NO}_x$  emissions require the combustion zone to be lean and very well mixed.
- (4) A measure of the mixedness in a combustor can be derived from time-averaged internal gas sample measurements.

The following are the major conclusions specific to the NASA swirl-can combustor:

- (5) At the operating conditions of interest, combustion in the module wakes is only slightly lean and not very well mixed, but the residence time is reasonably short.
- (6) Fuel evaporation times are much shorter than the gas residence times and "droplet combustion" does not occur.
- (7) Low  $\text{NO}_x$  emission can be achieved only by making the module wakes leaner and considerably better mixed.

## REFERENCES

1. "Should We Have A New Engine?" Jet Propulsion Lab. Publication No. SP43-17, Vol. 1, Cal. Tech., 1975.
2. "Control of Air Pollution from Aircraft and Aircraft Engines," Federal Register, Vol. 38, No. 136, Part II, July 17, 1973.
3. Heywood, J.B., and Mikus, T., "Parameters Controlling Nitric Oxide Emissions from Gas Turbine Combustors," Atmospheric Pollution by Aircraft Engines, NATO/AGARD Conference Proceedings No. 125, AGARD Propulsion and Energetic Panel 41st Meeting, London, April 9-13, 1973.
4. Niedzwiecki, R.W., and Jones, R.E., "Pollution Measurements of a Swirl-Can Combustor," AIAA Paper No. 72-1201, AIAA/SAE 8th Joint Propulsion Specialist Conference, New Orleans, November 29 - December 1, 1972.
5. Lavoie, G.A., Heywood, J.B., and Keck, J.C., "Experimental and Theoretical Study of Nitric Oxide Formation in Internal Combustion Engines," Comb. Sci. and Tech. Vol. 1, 1970, pp. 313-326.
6. Le Trung, Q., MacKay, D., Hirata, A., and Trass, O., "A Shock Tube Study of the Thermal Decomposition of Nitric Oxide," Comb. Sci. Tech., Vol. 10, 1975, pp. 155-162.
7. Baulch, D.L., Drysdale, D.D., Horne, D.G., and Lloyd, A.C., Evaluated Kinetic Data for High Temperature Reactions, Vol. 2, Butterworths, London, 1973.
8. Heywood, J.B., "Gas Turbine Combustor Modelling for Calculating Nitric Oxide Emissions," AIAA Paper No. 71-712, AIAA/SAE 7th Propulsion Joint Specialist Conference, Salt Lake City, June 14-18, 1971.
9. Westenberg, A.A., "Kinetics of NO and CO in Lean, Premixed Hydrocarbon-Air Flames," Comb. Sci. Tech., Vol. 4, 1971, pp. 59-64.
10. Morr, A., "A Model for Carbon Monoxide Emissions from Industrial Gas Turbine Engines," Ph.D. Thesis, M.I.T., February 1973.
11. Heywood, J.B., Fay, J.A., and Linden, L.H., "Jet Aircraft Air Pollutant Production and Dispersion," AIAA J., Vol. 9, 1971, pp. 841-850.
12. Corrsin, S., "Statistical Behavior of a Reacting Mixture in Isotropic Turbulence," Physics of Fluids, Vol. 1, 1958, pp. 42-47.
13. Flagan, R.C., and Appleton, J.P., "Statistical Turbulent Mixing Models Applied to Nitric Oxide Formation in Combustion," Fluid Mechanics Lab. Publications No. 73-10, M.I.T., 1973.



14. Anderson, D.C., "Effects of Premixing on Nitric Oxide Formation," NASA Technical Memo. No. TMX-68220, 1973.
15. Anderson, D., "Effects of Equivalence Ratio and Dwell Time on Exhaust Emissions from an Experimental Premixing Pre vaporizing Burner," NASA Technical Memo. No. TMX-71592, 1975.
16. Mularz, E.J., Wear, J.D. and Verbulecz, P.W., "Pollution Emissions from Single Swirl-Can Combustor Modules at Parametric Test Conditions," NASA TMX-3167, January 1975.
17. Heat Transfer Section publication nos. HTS/74/2 and HTS/74/3, Mech. Eng. Dept., Imperial College, 1974.
18. Prandtl, L., Essentials of Fluid Dynamics, Blackie and Son, London, 1952.
19. Komiya, K., "The Effects of Fuel Injector Characteristics on Fuel-Air Mixing in a Burner," Ph.D. Thesis, M.I.T., February, 1975.
20. Goldsmith, M., and Penner, S.S., "On the Burning of Single Drops in an Oxidizing Atmosphere," *Jet Propulsion*, Vol. 24, 1954, pp. 245-251.
21. Ranz, W.E., and Marshall, W.R., "Evaporation from Drops," *Chem. Eng. Prog.*, Vol. 48, 1952, p. 141.
22. Spalding, D.B., Some Fundamentals of Combustion, Butterworths, London, 1955.
23. Frazer, R.F., and Dombrowski, N., "Photographic Techniques for the Study of Movement," *J. Photog. Sci.*, Vol. 10, 1962, p. 155.
24. Wigg, L.D., "Drop Size Predictions for Twin Fluid Atomizers," *J. Inst. Fuel*, Vol. 37, 1964, pp. 500-505.
25. Hoult, D.P. and Weil, J.C., "Turbulent Plume in a Laminar Cross Flow," *Atm. Environment*, Vol. 6, 1972, pp. 513-531.
26. Spindt, R.S., "Air-Fuel Ratio from Exhaust Gas Analysis," SAE Paper No. 650507, Mid-Year Meeting, Chicago, May 17-21, 1965.



1. Report No. <b>NASA CR-2977</b>	2. Government Accession No.	3. Recipient's Catalog No.	
4. Title and Subtitle <b>NITRIC OXIDE FORMATION IN GAS TURBINE ENGINES: A THEORETICAL AND EXPERIMENTAL STUDY</b>		5. Report Date <b>April 1978</b>	6. Performing Organization Code
		8. Performing Organization Report No. <b>None</b>	10. Work Unit No.
7. Author(s) <b>Thomas Mikus, John B. Heywood, and R. Edward Hicks</b>		11. Contract or Grant No. <b>NGR-22-009-378</b>	
		13. Type of Report and Period Covered <b>Contractor Report</b>	
9. Performing Organization Name and Address <b>Massachusetts Institute of Technology Cambridge, Massachusetts 02139</b>		14. Sponsoring Agency Code	
		12. Sponsoring Agency Name and Address <b>National Aeronautics and Space Administration Washington, D. C. 20546</b>	
15. Supplementary Notes Final report, Project Manager, Edward J. Mularz, Propulsion Laboratory, U. S. Army R&T Laboratories (AVRADCOM), NASA Lewis Research Center, Cleveland, Ohio. Report was submitted as a thesis by the first author in partial fulfillment of the requirements for the degree Doctor of Philosophy to Massachusetts Institute of Technology in November 1975.			
16. Abstract <p>A model for predicting <math>\text{NO}_x</math> emissions from gas turbine combustors is presented. A modified Zeldovich kinetic scheme is used to predict nitric oxide formation in the burned gases. Non-uniformities in fuel-air ratio in the primary zone are accounted for by a distribution of fuel-air ratios. This is followed by one or more dilution zones in which a Monte Carlo calculation is employed to follow the mixing and dilution processes. Predictions of <math>\text{NO}_x</math> emissions are compared with various available experimental data, and satisfactory agreement is achieved. In particular, the model is applied to the NASA swirl-can modular combustor. The operating characteristics of this combustor which can be inferred from the modeling predictions are described. Parametric studies are presented which examine the influence of the modeling parameters on the <math>\text{NO}_x</math> emission level. Experimental work is reported further verifying this modeling application. A series of flow visualization experiments demonstrates the fuel droplet breakup and turbulent recirculation processes. A tracer experiment quantitatively follows the jets from the swirler as they move downstream and entrain surrounding gases. Techniques are developed for calculating both fuel-air ratio and degree of nonuniformity from measurements of <math>\text{CO}_2</math>, <math>\text{CO}</math>, <math>\text{O}_2</math>, and hydrocarbons. A burning experiment makes use of these techniques to map out the flow field in terms of local equivalence ratio and mixture nonuniformity.</p>			
17. Key Words (Suggested by Author(s)) <b>Combustor modeling Oxides of nitrogen Fuel-air ratio nonuniformities</b>		18. Distribution Statement <b>Unclassified - unlimited STAR category 07</b>	
19. Security Classif. (of this report) <b>Unclassified</b>	20. Security Classif. (of this page) <b>Unclassified</b>	21. No. of Pages <b>104</b>	22. Price* <b>A06</b>



**END**

**8.23.78**